

Preconditioned BFGS-based Uncertainty Quantification in elastic Full Waveform Inversion

Qiancheng Liu¹, Stephen Beller¹, Wenjie Lei¹, Daniel Peter², and Jeroen Tromp^{1,3}

¹Department of Geosciences, Princeton University, Princeton, NJ 08544, USA

²Division of Physical Sciences and Engineering, King Abdullah University of Science and Technology (KAUST), Thuwal, Saudi Arabia

³Program in Applied and Computational Mathematics, Princeton University, Princeton, NJ 08544, USA

2020

SUMMARY

Full Waveform Inversion (FWI) plays a vital role in reconstructing geophysical structures. The Uncertainty Quantification regarding the inversion results is equally important but has been missing out in most of the current geophysical inversions. Mathematically, uncertainty quantification is involved with the inverse Hessian (or the posterior covariance matrix), which is prohibitive in computation and storage for practical geophysical FWI problems. L-BFGS populates as the most efficient Gauss-Newton method; however, in this study, we empower it with the new possibility of accessing the inverse Hessian for uncertainty quantification in FWI. To facilitate the inverse-Hessian retrieval, we put together BFGS (essentially, full-history L-BFGS) with randomized singular value decomposition towards a low-rank approximation of the Hessian inverse. That the rank number equals the number of iterations makes this solution efficient and memory-affordable even for large-scale inversions. Also, based on the adjoint method, we formulate different diagonal Hessian initials as preconditioners and compare their performances in elastic FWI. We highlight our methods with the elastic Marmousi benchmark,

demonstrating the applicability of preconditioned BFGS in large-scale FWI and uncertainty quantification.

Key words: computational seismology, seismic tomography, waveform inversion, preconditioner, uncertainty quantification

1 INTRODUCTION

Seismic full-waveform inversion (FWI) acts as an essential toolset in characterizing the subsurface properties. FWI aims at estimating the “optimal” model by minimizing the data misfit between the simulated and the observed seismograms, most commonly, via iterative inversion in a least-squares sense (Lailly 1983; Tarantola 1984). Its ultimate goal is to understand the said properties from all the available information in the observed seismic measurements (Tromp 2019). Thanks to the developments and advances in data acquisition, high-performance computing and numerical simulation methods (Komatitsch & Tromp 1999b; Peter et al. 2011), FWI can constrain the seismic models with higher resolution increasingly. Successful applications of FWI across scales have been reported in global (French & Romanowicz 2014; Bozdağ et al. 2016; Fichtner et al. 2018; Lei et al. 2020), regional (Tape et al. 2010; Zhu et al. 2012; Krischer et al. 2018), exploration (Warner & Guasch 2016; Métivier et al. 2016), and medical-imaging (Bachmann & Tromp 2020; Guasch et al. 2020) cases. However, as an ill-posed inverse problem, FWI suffers from non-unique solutions owing to the limited data coverage and the uncertainties in measurements and theories. The uncertainty quantification in FWI is equally essential, but only a few solutions have been proposed in practical applications (Fichtner & Trampert 2011a,b; Zhu et al. 2016; Fichtner & Simutè 2018; Liu & Peter 2019, 2020; Thurin et al. 2019; Gebraad et al. 2019).

The optimization methods in FWI can be categorized into two families: deterministic and statistical. The deterministic methods, mainly referring to the gradient optimization-based ones (Pratt 1999; Virieux & Operto 2009), have been well developed in tackling challenges such as cycle-skipping (Warner & Guasch 2016; Métivier et al. 2016) and source-encoding (Tromp & Bachmann 2019). The latter methods, relying on statistical sampling such as Hamiltonian Monte Carlo (Duane et al. 1987), are theoretically preferable in FWI because they provide not

only the maximum a posteriori (MAP) model but also the statistic metrics for uncertainty quantification (Biswas & Sen 2017; Fichtner & Simutè 2018; Gebraad et al. 2019). The statistical family is often prohibitive for large-scale practical applications due to its costly computational expenses (Tarantola 2005). In contrast, the deterministic family popularizes in the FWI community due to its low cost and high efficiency. Tarantola (2005) unveils the hope for FWI and uncertainty quantification by deterministic optimization once the posterior covariance can be constructed for model appraisal (Tarantola & Valette 1982).

The posterior model covariance is closely related to the inverse data-misfit Hessian under the assumption of linearizable forward modeling and Gaussian model priors (Tarantola 2005). For large-scale applications involving millions of parameters, it becomes unfeasible to store, assemble, and analyze such huge matrices. To tackle this issue, Zhang & McMechan (1995) compress the data volume of classic inversion algorithms using least-squares QR factorization. Trampert et al. (2012) random-probe the tomographic models to estimate the resolution lengths of waveform tomography. Rawlinson et al. (2014) provide a recent review about uncertainty estimations in waveform inversion. Fichtner & van Leeuwen (2015) furthermore analyze the direction-dependent resolution lengths from the randomly sampled Hessian via autocorrelation. Bui-Thanh et al. (2013) approximate the posterior covariance matrix by eigendecomposing the data-misfit Hessian for its inverse with randomized singular-value decomposition (RSVD) (Liberty et al. 2007; Halko et al. 2011). Zhu et al. (2016) exploit the point-spread function (PSF) tests to improve the Hessian-computation efficiency. Luo (2012) and Liu et al. (2019) proposed to perform FWI with a memory-affordable vector-version square-root variable metric (SRVM) algorithm. Subsequently, Liu & Peter (2019) cascade SRVM and RSVD to efficiently probe the inverse Hessian for uncertainty quantification in FWI and then characterize the nonuniqueness of FWI by SRVM-based null-space shuttle (Thurin et al. 2019; Liu & Peter 2020).

In this paper, we explore the feasibility of a classic quasi-Newton method, BFGS (essentially, in full-memory L-BFGS) (Broyden 1970; Liu & Nocedal 1989), for the application of elastic FWI and uncertainty quantification. Similar to the SRVM-RSVD workflow (Liu & Peter 2020), we present a BFGS-RSVD approach to access and factorize the inverse Hessian. BFGS runs in the framework of L-BFGS. According to Nocedal & Wright (2006), L-BFGS is equiv-

alent to the BFGS algorithm if L-BFGS keeps the same initial Hessian and all the memories. Fortunately, FWI usually takes several or tens of iterations to converge. The resulting storage of full-memory L-BFGS vectors is affordable even for large-scale applications. The performance of BFGS in FWI may be closely related to the initial Hessian guess (Brossier et al. 2009; Métivier et al. 2013; Yang et al. 2018; Beller & Chevrot 2020). Thus, we investigate the performance of different diagonal approximations of the initial inverse Hessian and compare them in terms of FWI convergence rates and uncertainty quantification maps.

The purpose of this study is to bring together L-BFGS, Hessian-related preconditioners, and their roles in Uncertainty Quantification of FWI. The paper is organized as followed. We start with a brief review of the FWI optimization problem and recall the theory of the L-BFGS quasi-Newton algorithm. We continue with a presentation of potential *computationally cheap* diagonal preconditioners used as initial guesses of the L-BFGS approximation of the inverse Hessian. We then discuss the retrieval of the Hessian inverse after BFGS-based FWI has converged. Subsequently, we propose a BFGS-RSVD workflow to make faster and cheaper the BFGS-based Hessian retrieval. Finally, we verify our methods with numerical examples to demonstrate the applicability of preconditioned BFGS-based FWI for uncertainty quantification.

2 THEORIES & METHODS

2.1 BFGS in FWI

Seismic FWI aims at iteratively minimizing the misfit function $f(\mathbf{m}) = \|\mathbf{d} - \mathbf{d}_0\|_2^2$ between the observed and synthetic data \mathbf{d}_0 and \mathbf{d} respectively. In principle, an FWI consists of three consecutive steps: I) misfit and gradient computations, e.g., with the adjoint method (Tromp et al. 2005; Plessix 2006); II) search direction updated from the gradient by optimization methods (Liu & Nocedal 1989; Métivier et al. 2013; Liu et al. 2019); III) linear search, e.g., using the Wolfe conditions (Wolfe 1969; Nocedal & Wright 2006), along the search direction. In this section, we focus on the optimization algorithm BFGS (specifically, full-memory L-BFGS), discuss its applicability in FWI, and its potential in accessing the uncertainty quantification of the FWI results.

At iteration k , the quasi-Newton search direction \mathbf{p}_k is given by

$$\mathbf{p}_k = -\mathbf{B}_k \nabla f(\mathbf{m}_k), \quad (1)$$

with $\mathbf{g}_k = \nabla f(\mathbf{m}_k)$ being the gradient, and \mathbf{B}_k the inverse Hessian or its approximation. The gradient \mathbf{g}_k is efficiently computed using the adjoint-state method (Tromp et al. 2005). For practical applications, the direct computation and storage of the Hessian or its inverse are prohibitive. Instead, L-BFGS provides an efficient matrix-free and iterative approach, which first approximates the Hessian in a rank-two update

$$\mathbf{H}_{k+1} = \mathbf{H}_k + \frac{\mathbf{y}_k \mathbf{y}_k^T}{\mathbf{y}_k^T \mathbf{s}_k} - \frac{\mathbf{H}_k \mathbf{s}_k \mathbf{s}_k^T \mathbf{H}_k^T}{\mathbf{s}_k^T \mathbf{H}_k \mathbf{s}_k}, \quad (2)$$

with $\mathbf{y}_k = \mathbf{g}_{k+1} - \mathbf{g}_k$ and $\mathbf{s}_k = \mathbf{m}_{k+1} - \mathbf{m}_k$, and then applies the Sherman-Morrison formula to get the inverse Hessian

$$\mathbf{B}_{k+1} = \left(\mathbf{I} - \frac{\mathbf{s}_k \mathbf{y}_k^T}{\mathbf{y}_k^T \mathbf{s}_k} \right) \mathbf{B}_k \left(\mathbf{I} - \frac{\mathbf{y}_k \mathbf{s}_k^T}{\mathbf{y}_k^T \mathbf{s}_k} \right) + \frac{\mathbf{s}_k \mathbf{s}_k^T}{\mathbf{y}_k^T \mathbf{s}_k}, \quad (3)$$

from which we observe that \mathbf{B}_{k+1} remains in a matrix form, unfeasible in storage. L-BFGS, which approximates BFGS in a limited amount of memories regarding the past gradients and model updates, runs in a two-loop recursion

Algorithm 1 L-BFGS search direction computation

```

1:  $\mathbf{q} = \mathbf{g}_k$ 
2: for  $i \leftarrow k - 1$  to  $k - m$  do
3:    $r_i = 1/\mathbf{y}_i^T \mathbf{s}_i$ 
4:    $a_i = r_i \mathbf{s}_i^T \mathbf{q}$ 
5:    $\mathbf{q} = \mathbf{q} - a_i \mathbf{y}_i$ 
6: end for
7:  $\gamma_k = (\mathbf{s}_{k-1}^T \mathbf{y}_{k-1}) / (\mathbf{y}_{k-1}^T \mathbf{y}_{k-1})$ 
8:  $\mathbf{z} = \gamma_k \mathbf{B}_k^0 \mathbf{q}$ 
9: for  $i \leftarrow k - m$  to  $k - 1$  do
10:   $b_i = r_i \mathbf{y}_i^T \mathbf{z}$ 
11:   $\mathbf{z} = \mathbf{z} + \mathbf{s}_i (a_i - b_i)$ 
12: end for
13:  $\mathbf{z} = -\mathbf{z}$ 

```

with m being the memory value, and γ_k the scaling factor (Morales & Nocedal 2000). Alg. (1) outputs the scaled search direction $\mathbf{z} = -\gamma_k \mathbf{B}_k \mathbf{g}_k$ towards a local minimizer with linear memory requirement. Besides being efficient and inexpensive, this recursion has the advantage that the initial inverse Hessian \mathbf{B}_k^0 at iteration k is included but isolated from the two-loop recursion. γ_k attempts to estimate an effective scaling for $-\mathbf{B}_k \mathbf{g}_k$, so that a unit step length is accepted for most of the iterations. \mathbf{B}_k^0 opens a window for the preconditioner trials from different initial Hessian estimates.

Liu et al. (2019) and Liu and Peter (2019) discuss the feasibility of the Square-Root Variable Metric (SRVM) based FWI and uncertainty quantification. Both SRVM and BFGS belong to the family of quasi-Newton methods. They only differ in that SRVM originates from the Davidon-Fletcher-Powell (DFP) algorithm (Davidon 1959; Fletcher & Powell 1963), the dual of BFGS. Both in an iterative manner, while DFP casts a direct approximation to the Hessian inverse, BFGS first approximates the Hessian and then takes its inverse by the Sherman-Morison formula. Theoretically, we can identically retrieve the Hessian inverse from the BFGS-based FWI in a similar way. L-BFGS, a variant of BFGS, acts as the state-of-the-art optimiza-

tion algorithm for decades. Nocedal & Wright (2006) states that L-BFGS is equivalent to BFGS if all the memories are kept, while the initial guess of Hessian inverse stays unchanged. Theoretically, BFGS can capture the second-order derivative information from the start to the end without dropping histories. As a result, \mathbf{B}_k^0 becomes independent of iterations, so we can recast \mathbf{B}_k^0 as \mathbf{B}_0 . Thus, there is no need in updating the Hessian initial as FWI iterates, although Modrak & Tromp (2016) have illustrated that it is unnecessary to update the preconditioner for FWI within one frequency band regularly.

2.2 Preconditioners in BFGS

Ideally, the inverse Hessian in elastic FWI can be used to reforge the gradients to directly account for the parameter trade-offs as well as the source-receiver illumination (Pratt 1999; Virieux et al. 2009; Métivier et al. 2013; Yang et al. 2018). However, the explicit computation and storage of the Hessian and its inverse in the practical applications are prohibitive. FWI is formulated as a nonlinear minimization of the waveform mismatch between the observed and synthetic data via iterative inversion to account for the Hessian inverse indirectly. For large-scale problems (Fichtner et al. 2018; Lei et al. 2020), however, the gradients estimated by the adjoint method are also expensive, such that we can only afford a handful of iterations (Tromp 2019). As suggested in alg. (1), the inverse of an initial Hessian guess can be applied to mimic the inverse Hessian effects to partially improve the performance and reduce the cost of the computationally demanding nonlinear-optimization problems. Therefore, we firstly need the estimation of the initial Hessian, directly or indirectly.

Regarding the initial Hessian estimations, generally, there are three types of categories: I) Gauss-Newton; II) Point-spreading function; III) Diagonal Hessian. Category I) involves the Hessian update on the fly (Demanet et al. 2012; Métivier et al. 2013); Category II) is based on the point-spreading functions for an initial Hessian estimation (Zhu et al. 2016); Category III), which is the most popular in the geophysics community, constructs the initial Hessian diagonals using the adjoint methods (Claerbout 1971; Shin et al. 2008; Rickett 2003; Yang et al. 2018). Here we mainly focus on Category III) due to its effectiveness and easy implementation, which would be a good starting point to advance towards a more sophisticated algorithm such as L-BFGS for inverse Hessian construction.

We prefer the diagonal approach because it provides an efficient yet inexpensive and robust initial Hessian estimation. Given $\mathbf{J} = \delta\mathbf{d}/\delta\mathbf{m}$ as the first-order Fréchet derivative, the initial inverse Hessian \mathbf{B}_0 in Alg. (1) can be estimated as

$$\mathbf{B}_0 = [\text{diag}(\mathbf{J}^\dagger\mathbf{J}) + \lambda\mathbf{I}]^{-1} = (\mathbf{H}_0 + \lambda\mathbf{I})^{-1}, \quad (4)$$

in which $\mathbf{H}_0 = \text{diag}(\mathbf{J}^\dagger\mathbf{J})$ indicates the diagonalized Hessian initial, and the regularization term $\lambda\mathbf{I}$ exists for stabilization. For convenience in this study we call preconditioners the initial diagonal approximations of the Hessian although their inverses are what enter the applications.

We can account for the diagonal Hessian from two different views: the simple data illumination (Claerbout 1971; Shin et al. 2008; Rickett 2003) and the adjoint-state method (Yang et al. 2018). Each has two alternatives: consideration of only the source geometry or both the source and receiver geometries. Given an elastic FWI with interest in P- and S-wave velocities α and β , let us start from the well-known source-illumination map as

$$H_0 = \int \left(\frac{\partial\mathbf{v}}{\partial t} \right) \cdot \left(\frac{\partial\mathbf{v}}{\partial t} \right) dt, \quad (5)$$

in which \mathbf{v} is the source wavefield in particle velocities. We impose the same H_0 over the gradients of α and β to have our first kind of preconditioner $\mathbf{P}_1 = \{H_0, H_0\}$. Luo (2012) derives a similar form but called "ray density". Later we will show in our examples that even this kind of simplest preconditioner can lead to a significant improvement in FWI convergence. However, H_0 fails to account for the acquisition geometry, so we use a modified form of eq. (5) instead

$$\tilde{H}_0 = \left| \int \left(\frac{\partial\mathbf{v}}{\partial t} \right) \cdot \left(\frac{\partial\tilde{\mathbf{v}}}{\partial t} \right) dt \right|, \quad (6)$$

in which \mathbf{v} and $\tilde{\mathbf{v}}$ are the source and adjoint wavefields in particle velocities, respectively. Following Luo (2012), we take their absolute values in eq. (5) to ensure the positive definiteness of the approximate Hessian initial. As a result, similarly, our second kind of preconditioner is $\mathbf{P}_2 = \{\tilde{H}_0, \tilde{H}_0\}$. The computation of \mathbf{P}_1 only involves the source wavefield, yet that of \mathbf{P}_2 involves both the source and receiver wavefields. Therefore, it is expected to see a better performance of \mathbf{P}_2 than \mathbf{P}_1 in compensation for the uneven source-receiver data coverage.

Although \mathbf{P}_1 and \mathbf{P}_2 can be useful in FWI acceleration, the approximate "elastic" Hessian initials should be inclined to have better performance over those above due to the account of

inherent nonlinearity in elastic inversion. The mathematical derivations for the multi-parameter Hessian initials can be found in Appendix A. Eq. (A21) shows that the elastic Hessian initials can be given as

$$\begin{aligned} H_{\alpha\alpha} &= \int \left(\frac{\partial \mathbf{C}}{\partial \alpha} \mathbf{D} \mathbf{v} \right) \cdot \left(\frac{\partial \mathbf{C}}{\partial \alpha} \mathbf{D} \mathbf{v} \right) dt, \\ H_{\beta\beta} &= \int \left(\frac{\partial \mathbf{C}}{\partial \beta} \mathbf{D} \mathbf{v} \right) \cdot \left(\frac{\partial \mathbf{C}}{\partial \beta} \mathbf{D} \mathbf{v} \right) dt, \end{aligned} \quad (7)$$

where \mathbf{v} denotes the particle velocities of the source wavefield, \mathbf{C} the (α, β, ρ) related stiffness matrix, and \mathbf{D} the combination of differential operators. The details of \mathbf{C} and \mathbf{D} can be found after eq. (A7). The resulting preconditioner of the third kind can be expressed as $\mathbf{P}_3 = \{H_{\alpha\alpha}, H_{\beta\beta}\}$. Again, as discussed in eq. (A22) of Appendix A, we furthermore extend eq. (7) to account for the acquisition geometry as

$$\begin{aligned} \tilde{H}_{\alpha\alpha} &= \left| \int \left(\frac{\partial \mathbf{C}}{\partial \alpha} \mathbf{D} \mathbf{v} \right) \cdot \left(\frac{\partial \mathbf{C}}{\partial \alpha} \mathbf{D} \tilde{\mathbf{v}} \right) dt \right|, \\ \tilde{H}_{\beta\beta} &= \left| \int \left(\frac{\partial \mathbf{C}}{\partial \beta} \mathbf{D} \mathbf{v} \right) \cdot \left(\frac{\partial \mathbf{C}}{\partial \beta} \mathbf{D} \tilde{\mathbf{v}} \right) dt \right|, \end{aligned} \quad (8)$$

where \mathbf{v} and $\tilde{\mathbf{v}}$ denote the particle velocities of the source and adjoint wavefields, respectively. As a result, the preconditioner of the fourth kind $\mathbf{P}_4 = \{\tilde{H}_{\alpha\alpha}, \tilde{H}_{\beta\beta}\}$. Similarly, it is expected to see \mathbf{P}_4 outperforms \mathbf{P}_3 . As for the computational burden, if we compute the Hessian initial separately, \mathbf{P}_1 and \mathbf{P}_3 are at the cost of one wavefield simulation, and \mathbf{P}_2 and \mathbf{P}_4 are at the cost of one gradient computation. They are all cheap compared with the expensive FWI cost. When it comes to large-scale applications, we can furthermore reduce the Hessian costs to the minimal by computing them together with gradients. Also, for each positive-definite preconditioner, a large ratio between its maximum and minimum (similar to a large condition number) can result in numerical instability, which can be alleviated by smoothing and damping (Rickett 2003). Here we use the inverse of the smoothed, damped initial diagonal Hessians $diag(\mathbf{J}^\dagger \mathbf{J})$ in the forms of \mathbf{P}_1 , \mathbf{P}_2 , \mathbf{P}_3 , and \mathbf{P}_4 respectively, to take the role of \mathbf{B}_0 in Alg. (1).

2.3 Preconditioned BFGS-based Uncertainty Quantification

With the BFGS algorithm and its preconditioners provided, when elastic FWI converges after n iterations, \mathbf{B}_{n+1} can approximate the Hessian inverse from the past n histories (Tarantola 2005; Nocedal & Wright 2006). Following Liu & Peter (2019), we retrieve the Hessian inverse by

$$\mathbf{H}^{-1} = \mathbf{B}_{n+1} - \mathbf{B}_0 = (\mathbf{B}_{n+1}/\mathbf{B}_0 - \mathbf{I}) \mathbf{B}_0 \quad (9)$$

From alg. (1) we see that the reconstruction of \mathbf{B}_{n+1} involves \mathbf{B}_0 , \mathbf{s}_i , and \mathbf{y}_i ($i = 0, 1, \dots, n$). After the preconditioning with \mathbf{B}_0 in FWI, the wavefield related pieces of information are mainly embedded in $\mathbf{B}_{n+1}/\mathbf{B}_0$, which starts from \mathbf{I} for stabilization. Note that \mathbf{B}_0 has been estimated and kept, and $\mathbf{B}_{n+1}/\mathbf{B}_0$ rather than \mathbf{B}_{n+1} is retrieved from \mathbf{s}_i and \mathbf{y}_i .

The retrieval of \mathbf{B}_{n+1} from \mathbf{B}_0 , \mathbf{s}_i , and \mathbf{y}_i can be done with a unit pulse probing vector $\hat{\mathbf{e}}_j = (0, 0, \dots, 0, 1, 0, \dots, 0, 0)$ in which the unit pulse "1" locates at the target column (row) index j ($j = 1, \dots, M$, with M being the model size), but not in an efficient way. We can extract the j th row/column elements from \mathbf{B}_{n+1} in the following way

Algorithm 2 \mathbf{B}_{n+1} probing

```

1:  $\mathbf{q} = \hat{\mathbf{e}}_j$ 
2: for  $i \leftarrow n$  to 0 do
3:    $r_i = 1/\mathbf{y}_i^T \mathbf{s}_i$ 
4:    $a_i = r_i \mathbf{s}_i^T \mathbf{q}$ 
5:    $\mathbf{q} = \mathbf{q} - a_i \mathbf{y}_i$ 
6: end for
7:  $\mathbf{z} = \mathbf{B}_0 \mathbf{q}$ 
8: for  $i \leftarrow 0$  to  $n$  do
9:    $b_i = r_i \mathbf{y}_i^T \mathbf{z}$ 
10:   $\mathbf{z} = \mathbf{z} + \mathbf{s}_i (a_i - b_i)$ 
11: end for
12:  $\mathbf{z} = \mathbf{z} - \mathbf{B}_0 \mathbf{z}$ 

```

This two-loop algorithm outputs the matrix-vector product $\mathbf{z} = (\mathbf{B}_{n+1} - \mathbf{B}_0) \hat{\mathbf{e}}$. However, Alg. (2) is not flexible in arbitrary element extraction. For example, given a model of size M , we need M such operations in extracting the \mathbf{B}_{n+1} diagonals, which is expensive for the uncertainty quantification of large-scale applications. Fortunately, randomized SVD (Liberty et al. 2007; Halko et al. 2011) gives the hope to efficiently eigendecompose large matrices, especially for those with the low-rank property. The method proposed in Halko et al. (2011) can probe a matrix only with one set of random vectors in a much smoother implementation. Given an elastic FWI at model size M converges after N_r iterations. Although $\mathbf{B} = \mathbf{H}^{-1} =$

$\mathbf{B}_{n+1} - \mathbf{B}_0$ can span a $M \times M$ full matrix prohibitively in computation and storage, we probe it simply with a set of $M \times N_r$ independent random vectors \mathbf{X} , similar to that in Liu & Peter (2019). The single-pass randomized SVD allows an efficient eigendecomposition of matrix \mathbf{B} of $M \times M$ as follows

Algorithm 3 Single-pass randomised SVD algorithm

- 1: $\mathbf{E} = \mathbf{B}\mathbf{X}$ ▷ Sampling \mathbf{B} with \mathbf{X}
 - 2: $\mathbf{QR} = \mathbf{E}$ ▷ QR decomposition on \mathbf{E}
 - 3: $\Omega(\mathbf{Q}^T\mathbf{X}) = \mathbf{Q}^T\mathbf{E}$ ▷ Solve for Ω
 - 4: $\mathbf{U}\Lambda\mathbf{U}^T = \Omega$ ▷ SVD on Ω
 - 5: $\mathbf{V} = \mathbf{Q}\mathbf{U}$
 - 6: $\mathbf{Z} = \mathbf{V}\Lambda\mathbf{V}^T$
-

When setting the target as $\mathbf{B} = \mathbf{H}^{-1}$, we use \mathbf{X} to probe $\mathbf{B}_{n+1} - \mathbf{B}_0$, yielding $\mathbf{E} = \mathbf{B}_{n+1}\mathbf{X} - \mathbf{B}_0\mathbf{X}$. Here \mathbf{X} consists of N_r independent random vectors, with $N_r \ll M$. Note that we never write out the full matrix of \mathbf{B} . We simply need to replace the \hat{e}_j in alg. (2) with x_k , ($x_k \in \mathbf{X}$, and $k = 1, \dots, N_r$), to have \mathbf{E} . When performing the QR decomposition, we only need to keep \mathbf{Q} of size $M \times N_r$. Then, except that \mathbf{V} is of size $M \times N_r$, all the other matrices are of size $N_r \times N_r$. We recall the N_r denotes the iteration number. Finally, alg. (3) outputs the Hessian inverse in an SVD form as

$$\mathbf{H}^{-1} = \mathbf{V}\Lambda\mathbf{V}^T, \tag{10}$$

with \mathbf{V} being an $M \times N_r$ eigenvector matrix, and Λ the eigenvalue matrix of N_r diagonal entries. Eq. (10) provides a convenient way to access arbitrary elements out of the Hessian inverse.

For a linearized inverse problem with Gaussian priors, the relation between the model prior and posterior covariance matrices \mathbf{C}_M and \mathbf{C}_m can be expressed as (Tarantola 2005; Rawlinson et al. 2014)

$$\mathbf{C}_M = (\mathbf{J}^\dagger\mathbf{C}_d^{-1}\mathbf{J} + \varepsilon\mathbf{C}_m^{-1})^{-1}, \tag{11}$$

where \mathbf{J} denotes the Jacobian matrix, \mathbf{C}_d the data covariance matrix, and ε a scaling factor.

Following Liu & Peter (2019), we choose to modify eq. (11) as

$$\mathbf{C}_M \approx \mathbf{C}_m^{1/2} \left(\mathbf{C}_m^{1/2} \mathbf{J}^\dagger \mathbf{C}_d^{-1} \mathbf{J} \mathbf{C}_m^{1/2} \right)^{-1} \mathbf{C}_m^{1/2} = \mathbf{C}_m^{1/2} \mathbf{H}^{-1} \mathbf{C}_m^{1/2}. \quad (12)$$

In doing so, $\mathbf{C}_m^{1/2}$ will appear as a transform matrix along with \mathbf{J} and \mathbf{J}^\dagger , yielding the approximated Hessian inverse as

$$\mathbf{H}^{-1} = \left(\mathbf{C}_m^{1/2} \mathbf{J}^\dagger \mathbf{C}_d^{-1} \mathbf{J} \mathbf{C}_m^{1/2} \right)^{-1}, \quad (13)$$

As a result, we have

$$\mathbf{C}_M \approx \mathbf{C}_m^{1/2} \mathbf{V} \mathbf{\Lambda} \mathbf{V}^T \mathbf{C}_m^{1/2}, \quad (14)$$

which shows that $\mathbf{C}_M^{1/2} \approx \mathbf{C}_m^{1/2} \mathbf{V} \mathbf{\Lambda}^{1/2} \mathbf{V}^T \mathbf{C}_m^{1/2}$ is very handy to access as well. \mathbf{C}_M and \mathbf{C}_m can be used for the samplings of prior and posterior distributions (Bui-Thanh et al. 2013; Zhu et al. 2016; Liu & Peter 2019) and the model null-space (Liu & Peter 2020). We refer to the papers aforementioned for more details about these topics. $\mathbf{C}_m^{1/2}$ can be estimated from the information of geology, well logs, or seismic imaging (Fomel & Claerbout 2003). Here, we simply set the \mathbf{C}_m as an identify matrix \mathbf{I} . The square-root diagonals of \mathbf{C}_M , known as the standard deviation, provides a quantitative measure of the posterior distribution (Tarantola 2005). We can also see from eqs (12) and (14) that given a simple \mathbf{C}_m , the main features of \mathbf{C}_M are reflected by \mathbf{H}^{-1} . The access to \mathbf{H}^{-1} via preconditioned-BFGS is the focus of this paper.

3 NUMERICAL EXAMPLES

We demonstrate the methods above with the isotropic elastic Marmousi benchmark with the parametrization of P- and S-wave velocities and density. We only account for the P- and S-wave velocities V_p and V_s but fix the density in the inversion due to its low-sensitivity in FWI (Virieux & Operto 2009; Blom et al. 2017). In this part, we aim to show the feasibility of BFGS and preconditioned-BFGSs in elastic FWI, and compare them in terms of convergence rates and uncertainty quantification maps.

3.1 2D elastic Marmousi benchmark

The 2D elastic Marmousi benchmark (Martin et al. 2006) is 9200 m long and 3000 m deep, which is popular in the community of exploration geophysics due to its substantial structure complexities and velocity variations that pose great challenges of nonlinearity in FWI. Fig. 1 shows the true and initial models, respectively. Fig. 1b is smoothed from Fig. 1a with a Gaussian blur wide enough to remove discontinuities and distort traveltimes. We run the forward and adjoint modelings with SPECFEM2D (Komatitsch & Vilotte 1998; Komatitsch & Tromp 1999a), with absorbing boundaries (Stacey 1988; Komatitsch & Martin 2007) around to mimic wavefield propagation in an infinite space. The observation system located 10 m underground consists of evenly-distributed 32 shots between 279 m and 8921 m, and 500 sensors between 100 m and 9100 m, respectively. The source time function is a Ricker wavelet of 4 Hz peak frequency. We manage the FWI workflow with SeisFlows (Modrak & Tromp 2016).

We start from running the BFGS-based elastic FWI with full-memory L-BFGS. To validate the effectiveness of BFGS in FWI, we compare its inversion results in Fig. 2b with those by L-BFGS of 5 memories in Fig. 2a ("5" is a commonly used L-BFGS memory value). We see that they yield almost similar inverted V_P and V_S images. Fig. 3 further compares the convergence behaviors of BFGS and L-BFGS based FWIs in terms of normalized data- and model- misfits. It shows that BFGS has a faster convergence rate than L-BFGS but at the price of using the full-history memory of vectors s_i and y_i mentioned above. Similar L-BFGS and SRVM comparison can also be seen from Liu et al. (2019), and SRVM resembles BFGS in keeping all the memories. Fortunately, s_i and y_i are of the model size, and the storage of them increases linearly with iterations. Even so, we do not mean that BFGS outperforms L-BFGS. Generally, the inverse problems in geophysical applications with high nonlinearity, such as the salt-body model, benefit more from lower memory values (Modrak & Tromp 2016). However, we can take some measures to alleviate the nonlinearity, such as using multi-scale inversion (Bunks et al. 1995), adaptive waveform inversion (Warner & Guasch 2016), or optimal-transport metrics (Métivier et al. 2016). Also, it is worth mentioning that one main target of this research is for applications of global waveform tomography, which often settle quickly into superlinear convergence (Tromp 2019).

The preconditioners can accelerate FWI. Regarding the preconditioners mentioned above, P1

and P3 only need the forward wavefield while P2 and P4 involve both the source/adjoint wavefields. All the preconditioners are prepared before FWI. Smoothing and damping with trials and errors are required to avoid the problem of numerical instability. Fig. 4 shows the inversion results of preconditioned BFGS-based FWIs with P1, P2, P3, P4, respectively. The comparison between Figs 2b and 4 indicates that the preconditioned BFGSs perform almost identical, or even better than purely BFGS in driving waveform tomography. The convergence comparisons in Fig. 5 further highlight the significant computational savings, thanks to the preconditioners. Fig. 5a shows that P3 and P4 outperform P1 and P2, respectively, in reaching similar data misfits but with fewer iterations, as expected before. These cross-comparisons stress the importance of accounting for the limited acquisition geometry in preconditioner estimations.

Besides the stored preconditioners, we keep the groups of \mathbf{s}_i and \mathbf{y}_i vectors accordingly for inverse Hessian reconstructions. Although with full-memory histories, \mathbf{s}_i and \mathbf{y}_i do not produce enormous storage burdens because they are of model size with linear memory requirements. When accessing the approximate inverse Hessian, we only fetch small segments of the stored files into memory per operation using the memory-map techniques, e.g., with MemMap in NumPy, to mitigate the peak memory cost. Afterwards, we can factorize the inverse Hessian by running randomized SVD over the stored preconditioner and \mathbf{s}_i and \mathbf{y}_i . Note that in this process, we never write out the full matrix of the Hessian inverse thanks to the power of randomized SVD. As discussed before and in Liu & Peter (2019), the rank of the approximate inverse Hessian equals the number of iterations N_{iter} . The resulting benefit is that we only need N_{iter} such independent random vectors of model size for the random probing $\mathbf{E} = \mathbf{Z}\mathbf{X}$ to kick off alg. (3), which subsequently outputs the Hessian inverse in an SVD form. Note that the eigen-order number of the factorized matrix is the same as the iteration number.

Shown on the top of Figs. 6~10 are the eigen-spectrums of the inverse Hessians from the BFGS-based elastic FWIs. Each of them starts from values with similar magnitudes but ends differently depending on the level of convergence. Their corresponding eigenvector groups are displayed following each eigen-spectrum. Each group has five eigenvectors of increasing eigen-orders, including the 1st, 5th, 10th, 20th, and the last one. Note that eigenvectors per group are orthogonal. In each eigenvector group, we see that as the eigen-order increases, the energies begin to move up towards the observation system. We can get to understand this

tendency of the energy moving from the inverse of the Hessian inverse \mathbf{B} , i.e., the Hessian \mathbf{H} , whose eigen-energies fade away from the observation system as the eigen-order increases (Bui-Thanh et al. 2013; Zhu et al. 2016). Another intriguing thing we observe is that Fig. 10f has some random noises. When looking at its eigen-spectrum in Fig. 10a, we reason this as rank deficiency. It means that the actual rank of this matrix is less than the pre-estimated number, and we can safely truncate the SVD to save storage.

With the inverse Hessians being in SVD forms, we can efficiently extract their standard deviations for Uncertainty Quantification maps, as shown in Fig. 11. From an overview, they look similar and the features of the uncertainty maps resemble those by SRVM-based FWI (Liu & Peter 2019) and Ensemble Kalman Filter (EnKF) method (Thurin et al. 2019). Noticeable is that the methods reported here are based upon the most popular Quasi-Newton method L-BFGS, and without any high additional cost introduced. For a physical explanation about the uncertainty maps, again, we can start the understandings from the data coverage, which directly reflects the Hessian. From a global view, the data coverage decreases with the geometrical spreading; from a specific view, a high-velocity anomaly may bend the energy away from passage. We can thus infer that the appearance of the uncertainty maps should counteract the Hessian characteristics. The uncertainty maps in Fig. 11 reflect some features of the inverse Hessian: 1) the uncertainty increases as data coverage decreases; 2) the high-velocity structures are often with relatively high uncertainties, especially for the two salts at the corners. In short, the uncertainty map shines that the model space with more data coverage will have more information gains or fewer uncertainties. Note that for some very marginal areas (e.g., the absorbing layers, the very bottom corners), their uncertainties appear to be zero. We reason that our method can not evaluate uncertainties for areas where the Fréchet kernels are always zero, as explained in Kennett et al. (1988) and Rawlinson et al. (2014).

For a detailed investigation of the uncertainty maps, we first look at Fig. 11 horizontally to compare the V_p row with the V_s row, seeing that the V_p model usually has stronger uncertainties than V_s . We reason this from the perspective that in the elastic isotropic media, the radiation pattern of V_p is isotropic while that of V_s is far-offset dominant. FWI favors the far-offset data because it can produce gradients of lower-wavenumber than the near-offset. The lower-wavenumber components, usually with stronger amplitudes, can help FWI get rid of lo-

cal minima to some extent. Then, we look at Fig. 11 vertically to compare the uncertainty maps from BFGS-based FWI with no preconditioner and different preconditioners. We notice that all the preconditioners in BFGS bring out almost identical V_p and V_s maps but with different computational savings. Generally, the specific Hessians from the adjoint method outperform those purely from the data illumination, and the Hessians considering the recording geometry outperform those not. Among them, P4 stands out as the best with the most reasonable uncertainty maps in Fig. 11e, especially for the parts around the salt bodies.

When looking into the detailed structures, we notice that Fig. 11e differs from the others, especially in the area of central faults (1km~2km in depth, 4km~7km in width). In this area, we see that the uncertainty maps of the others remain in the pattern of high-velocity structures, while that of Fig. 11e has been basically "shattered". This is a good sign of better data constraint around this area thanks to more information gain from the data. We can understand it from the iterative approximation of the inverse Hessian, which starts from the level of good data coverage towards the level of poor coverage. Once a level of good coverage have been well settled, the inverse Hessian estimation sets off towards next level, iteratively. As a result, the maximum of uncertainties will increase. This understanding can also explain the differences in the color-bar ranges. Among them, Fig. 11e has the largest range, while Figs 11c and 11d the similarly smallest. We reason that FWIs in Figs 11c and 11d meet the stopping criterions a bit early. We can also recall Fig. 5 to see that although the data misfits of BFGS & P2 and BFGS & P3 look fine, their final model misfits are larger than others. Note that we do not mean that BFGS & P2 and BFGS & P3 underperform the others in uncertainty quantification of FWI because their performances may involve different factors, such as the tuning of parameters. All the preconditioned-BFGSs bring in considerable speedups in FWI and yield reasonable accompanying uncertainty maps. Finally, it worths mentioning that the preconditioned-BFGS algorithms we demonstrate here are strictly based upon the standard FWI framework. There is no arising expensive cost in computation and storage before, during, and after waveform inversion. This advantage makes our methods fully scalable towards the exascale geophysical applications, e.g., the global-scale waveform inversion (Bozdağ et al. 2016; Fichtner et al. 2018; Lei et al. 2020) and uncertainty quantification.

4 CONCLUSIONS & DISCUSSIONS

Uncertainties inherently exist in inverse geophysical problems, such as waveform tomography, due to limitations in observations and theories. L-BFGS has become the most popular optimization method in applied mathematics, including seismic waveform tomography. We have presented that BFGS (in full-memory L-BFGS) has the potential for Uncertainty Quantification in FWI. Also, the well-considered preconditioners can help gain significant computational savings but yield the same, or even better, inversion results. The estimation of the uncertainty maps only requires to store the related preconditioner and two vectors y and s in L-BFGS. Because BFGS takes part in the inversion process thoroughly, the stored vectors inherently capture the multi-parameter information from the initial model to the inverted. The marriage between BFGS and randomized SVD can significantly facilitate the inverse Hessian retrieval, from which the standard deviations provide a straightforward view for evaluation of inversion convergence and uncertainties. The presented methods are strictly based on the standard FWI workflow but allow us to further extend to the Bayesian framework, even with the assumptions of the linearized forward modeling solvers and the Gaussian distributed model priors. This BFGS-based FWI & Uncertainty Quantification workflow is fully scalable, which may favor the upcoming exascale scientific applications.

5 ACKNOWLEDGEMENTS

The authors are grateful to Frederik J. Simons for inspiring discussions. This work was supported by ...

REFERENCES

- Bachmann, E. & Tromp, J., 2020. Source encoding for viscoacoustic ultrasound computed tomography, *The Journal of the Acoustical Society of America*, **147**(5), 3221–3235.
- Baysal, E., Kosloff, D. D., & Sherwood, J. W., 1983. Reverse time migration, *Geophysics*, **48**(11), 1514–1524.
- Beller, S. & Chevrot, S., 2020. Probing depth and lateral variations of upper-mantle seismic anisotropy from full-waveform inversion of teleseismic body-waves, *Geophysical Journal International*, **222**(1), 352–387.

- Biswas, R. & Sen, M., 2017. 2d full-waveform inversion and uncertainty estimation using the reversible jump hamiltonian monte carlo, in *SEG Technical Program Expanded Abstracts 2017*, pp. 1280–1285, Society of Exploration Geophysicists.
- Blom, N., Boehm, C., & Fichtner, A., 2017. Synthetic inversions for density using seismic and gravity data, *Geophysical Journal International*, **209**(2), 1204–1220.
- Bozdağ, E., Peter, D., Lefebvre, M., Komatitsch, D., Tromp, J., Hill, J., Podhorszki, N., & Pugmire, D., 2016. Global adjoint tomography: first-generation model, *Geophysical Journal International*, **207**(3), 1739–1766.
- Brossier, R., Operto, S., & Virieux, J., 2009. Seismic imaging of complex onshore structures by 2d elastic frequency-domain full-waveform inversion, *Geophysics*, **74**(6), WCC105–WCC118.
- Broyden, C. G., 1970. The convergence of a class of double-rank minimization algorithms 1. general considerations, *IMA Journal of Applied Mathematics*, **6**(1), 76–90.
- Bui-Thanh, T., Ghattas, O., Martin, J., & Stadler, G., 2013. A computational framework for infinite-dimensional Bayesian inverse problems Part i: The linearized case, with application to global seismic inversion, *SIAM Journal on Scientific Computing*, **35**(6), A2494–A2523.
- Bunks, C., Saleck, F. M., Zaleski, S., & Chavent, G., 1995. Multiscale seismic waveform inversion, *Geophysics*, **60**(5), 1457–1473.
- Chen, K. & Sacchi, M. D., 2017. Elastic least-squares reverse time migration via linearized elastic full-waveform inversion with pseudo-hessian preconditioning elastic lsrtm, *Geophysics*, **82**(5), S341–S358.
- Claerbout, J. F., 1971. Toward a unified theory of reflector mapping, *Geophysics*, **36**(3), 467–481.
- Davidon, W. C., 1959. Variable metric method for minimization, *A.E.C. Research and Development Report*, **ANL-5990**.
- Demanet, L., Létourneau, P.-D., Boumal, N., Calandra, H., Chiu, J., & Snelson, S., 2012. Matrix probing: a randomized preconditioner for the wave-equation hessian, *Applied and Computational Harmonic Analysis*, **32**(2), 155–168.
- Duane, S., Kennedy, A. D., Pendleton, B. J., & Roweth, D., 1987. Hybrid monte carlo, *Physics letters B*, **195**(2), 216–222.
- Fichtner, A. & Simutè, S., 2018. Hamiltonian monte carlo inversion of seismic sources in complex media, *Journal of Geophysical Research: Solid Earth*, **123**(4), 2984–2999.
- Fichtner, A. & Trampert, J., 2011a. Hessian kernels of seismic data functionals based upon adjoint techniques, *Geophysical Journal International*, **185**(2), 775–798.
- Fichtner, A. & Trampert, J., 2011b. Resolution analysis in full waveform inversion, *Geophysical Journal International*, **187**(3), 1604–1624.
- Fichtner, A. & van Leeuwen, T., 2015. Resolution analysis by random probing, *Journal of Geophysical*

- Research: Solid Earth*, **120**(8), 5549–5573.
- Fichtner, A., van Herwaarden, D.-P., Afanasiev, M., Simutè, S., Krischer, L., Çubuk-Sabuncu, Y., Taymaz, T., Colli, L., Saygin, E., Villaseñor, A., et al., 2018. The collaborative seismic earth model: generation 1, *Geophysical research letters*, **45**(9), 4007–4016.
- Fletcher, R. & Powell, M. J., 1963. A rapidly convergent descent method for minimization, *The computer journal*, **6**(2), 163–168.
- Fomel, S. & Claerbout, J. F., 2003. Multidimensional recursive filter preconditioning in geophysical estimation problems, *Geophysics*, **68**(2), 577–588.
- French, S. & Romanowicz, B., 2014. Whole-mantle radially anisotropic shear velocity structure from spectral-element waveform tomography, *Geophysical Journal International*, **199**(3), 1303–1327.
- Gebraad, L., Boehm, C., & Fichtner, A., 2019. Bayesian elastic full-waveform inversion using hamiltonian monte carlo, *EarthArXiv*, p. qftn5.
- Guasch, L., Agudo, O. C., Tang, M.-X., Nachev, P., & Warner, M., 2020. Full-waveform inversion imaging of the human brain, *NPJ digital medicine*, **3**(1), 1–12.
- Halko, N., Martinsson, P.-G., & Tropp, J. A., 2011. Finding structure with randomness: Probabilistic algorithms for constructing approximate matrix decompositions, *SIAM review*, **53**(2), 217–288.
- Kennett, B., Sambridge, M., & Williamson, P., 1988. Subspace methods for large inverse problems with multiple parameter classes, *Geophysical Journal International*, **94**(2), 237–247.
- Komatitsch, D. & Martin, R., 2007. An unsplit convolutional Perfectly Matched Layer improved at grazing incidence for the seismic wave equation, *Geophysics*, **72**(5), SM155–SM167.
- Komatitsch, D. & Tromp, J., 1999a. Introduction to the spectral element method for three-dimensional seismic wave propagation, *Geophysical Journal International*, **139**(3), 806–822.
- Komatitsch, D. & Tromp, J., 1999b. Introduction to the spectral element method for three-dimensional seismic wave propagation, *Geophysical journal international*, **139**(3), 806–822.
- Komatitsch, D. & Vilotte, J. P., 1998. The spectral-element method: an efficient tool to simulate the seismic response of 2D and 3D geological structures, *Bull. seism. Soc. Am.*, **88**(2), 368–392.
- Krischer, L., Fichtner, A., Boehm, C., & Igel, H., 2018. Automated large-scale full seismic waveform inversion for north america and the north atlantic, *Journal of Geophysical Research: Solid Earth*, **123**(7), 5902–5928.
- Lailly, P., 1983. The seismic inverse problem as a sequence of before-stack migrations, in *Proceedings of the Conference on Inverse Scattering, Theory and Application Expanded Abstracts*, pp. 206–220, Society of Industrial and Applied Mathematics, Philadelphia, PA, USA.
- Lei, W., Ruan, Y., Bozdağ, E., Peter, D., Lefebvre, M., Komatitsch, D., Tromp, J., Hill, J., Podhorszki, N., & Pugmire, D., 2020. Global adjoint tomography—model glad-m25, *Geophysical Journal International*, **223**(1), 1–21.

- Liberty, E., Woolfe, F., Martinsson, P.-G., Rokhlin, V., & Tygert, M., 2007. Randomized algorithms for the low-rank approximation of matrices, *Proceedings of the National Academy of Sciences*, **104**(51), 20167–20172.
- Liu, D. C. & Nocedal, J., 1989. On the limited memory BFGS method for large scale optimization, *Mathematical programming*, **45**(1), 503–528.
- Liu, Q. & Peter, D., 2019. Square-root variable metric based elastic full-waveform inversion—part 2: uncertainty estimation, *Geophysical Journal International*, **218**(2), 1100–1120.
- Liu, Q. & Peter, D., 2020. Square-root variable metric-based nullspace shuttle: A characterization of the nonuniqueness in elastic full-waveform inversion, *Journal of Geophysical Research: Solid Earth*, **125**(2), e2019JB018687.
- Liu, Q., Peter, D., & Tape, C., 2019. Square-root variable metric based elastic full-waveform inversion—part 1: theory and validation, *Geophysical Journal International*, **218**(2), 1121–1135.
- Luo, Y., 2012. Seismic imaging and inversion based on spectral-element and adjoint methods, *Ph.D. thesis*.
- Métivier, L., Brossier, R., Virieux, J., & Operto, S., 2013. Full waveform inversion and the truncated Newton method, *SIAM Journal on Scientific Computing*, **35**(2), B401–B437.
- Métivier, L., Brossier, R., Mérigot, Q., Oudet, E., & Virieux, J., 2016. Measuring the misfit between seismograms using an optimal transport distance: Application to full waveform inversion, *Geophysical Supplements to the Monthly Notices of the Royal Astronomical Society*, **205**(1), 345–377.
- Modrak, R. & Tromp, J., 2016. Seismic waveform inversion best practices: regional, global and exploration test cases, *Geophysical Journal International*, **206**(3), 1864–1889.
- Morales, J. L. & Nocedal, J., 2000. Automatic preconditioning by limited memory quasi-newton updating, *SIAM Journal on Optimization*, **10**(4), 1079–1096.
- Nocedal, J. & Wright, S., 2006. *Numerical Optimization*, Springer Series in Operations Research and Financial Engineering, Springer-Verlag, 2nd edn.
- Peter, D., Komatitsch, D., Luo, Y., Martin, R., Le Goff, N., Casarotti, E., Le Loher, P., Magnoni, F., Liu, Q., Blitz, C., et al., 2011. Forward and adjoint simulations of seismic wave propagation on fully unstructured hexahedral meshes, *Geophysical Journal International*, **186**(2), 721–739.
- Plessix, R., 2006. A review of the adjoint-state method for computing the gradient of a functional with geophysical applications, *Geophys. J. Int.*, **167**, 495–503.
- Pratt, R. G., 1999. Seismic waveform inversion in the frequency domain, part 1: Theory and verification in a physical scale model, *Geophysics*, **64**(3), 888–901.
- Rawlinson, N., Fichtner, A., Sambridge, M., & Young, M. K., 2014. Chapter one-seismic tomography and the assessment of uncertainty, *Advances in Geophysics*, **55**, 1–76.
- Rickett, J. E., 2003. Illumination-based normalization for wave-equation depth migration, *Geophysics*,

- 68(4), 1371–1379.
- Shin, C., Jang, S., & Min, D.-J., 2008. Improved amplitude preservation for prestack depth migration by inverse scattering theory, *Geophysical prospecting*, **49**(5), 592–606.
- Stacey, R., 1988. Improved transparent boundary formulations for the elastic-wave equation, *Bulletin of the Seismological Society of America*, **78**(6), 2089–2097.
- Tape, C., Liu, Q., Maggi, A., & Tromp, J., 2010. Seismic tomography of the southern california crust based on spectral-element and adjoint methods, *Geophysical Journal International*, **180**(1), 433–462.
- Tarantola, A., 1984. Inversion of seismic reflection data in the acoustic approximation, *Geophysics*, **49**, 1259–1266.
- Tarantola, A., 1988. Theoretical background for the inversion of seismic waveforms, including elasticity and attenuation, in *Scattering and attenuations of seismic waves, part i*, pp. 365–399, Springer.
- Tarantola, A., 2005. *Inverse problem theory and methods for model parameter estimation*, Society for Industrial and Applied Mathematics, Philadelphia, Pennsylvania, USA.
- Tarantola, A. & Valette, B., 1982. Generalized nonlinear inverse problems solved using the least squares criterion, *Reviews of Geophysics*, **20**(2), 219–232.
- Thurin, J., Brossier, R., & Métivier, L., 2019. Ensemble-based uncertainty estimation in full waveform inversion, *Geophysical Journal International*, **219**(3), 1613–1635.
- Trampert, J., Fichtner, A., & Ritsema, J., 2012. Resolution tests revisited: the power of random numbers, *Geophysical Journal International*, **192**(2), 676–680.
- Tromp, J., 2019. Seismic wavefield imaging of earth’s interior across scales, *Nature Reviews Earth & Environment*, pp. 1–14.
- Tromp, J. & Bachmann, E., 2019. Source encoding for adjoint tomography, *Geophysical Journal International*, **218**(3), 2019–2044.
- Tromp, J., Tape, C., & Liu, Q., 2005. Seismic tomography, adjoint methods, time reversal and banana-doughnut kernels, *Geophysical Journal International*, **160**(1), 195–216.
- Vigh, D., Jiao, K., Watts, D., & Sun, D., 2014. Elastic full-waveform inversion application using multicomponent measurements of seismic data collection, *Geophysics*, **79**(2), R63–R77.
- Virieux, A. & Operto, S., 2009. An overview of full-waveform inversion in exploration geophysics, *Geophysics*, **74**(6), WCC1–WCC26.
- Virieux, J., Operto, S., Ben-Hadj-Ali, H., Brossier, R., Etienne, V., Sourbier, F., Giraud, L., & Haidar, A., 2009. Seismic wave modeling for seismic imaging, *The Leading Edge*, **28**(5), 538–544.
- Warner, M. & Guasch, L., 2016. Adaptive waveform inversion: Theory, *Geophysics*, **81**(6), R429–R445.
- Wolfe, P., 1969. Convergence conditions for ascent methods, *SIAM review*, **11**(2), 226–235.
- Yang, P., Brossier, R., Métivier, L., Virieux, J., & Zhou, W., 2018. A time-domain preconditioned truncated newton approach to visco-acoustic multiparameter full waveform inversion, *SIAM Journal*

on Scientific Computing, **40**(4), B1101–B1130.

Zhang, J. & McMechan, G. A., 1995. Estimation of resolution and covariance for large matrix inversions, *Geophysical Journal International*, **121**(2), 409–426.

Zhu, H., Bozdağ, E., Peter, D., & Tromp, J., 2012. Structure of the european upper mantle revealed by adjoint tomography, *Nature Geoscience*, **5**(7), 493–498.

Zhu, H., Li, S., Fomel, S., Stadler, G., & Ghattas, O., 2016. A Bayesian approach to estimate uncertainty for full-waveform inversion using a priori information from depth migration, *Geophysics*, **81**(5), R307–R323.

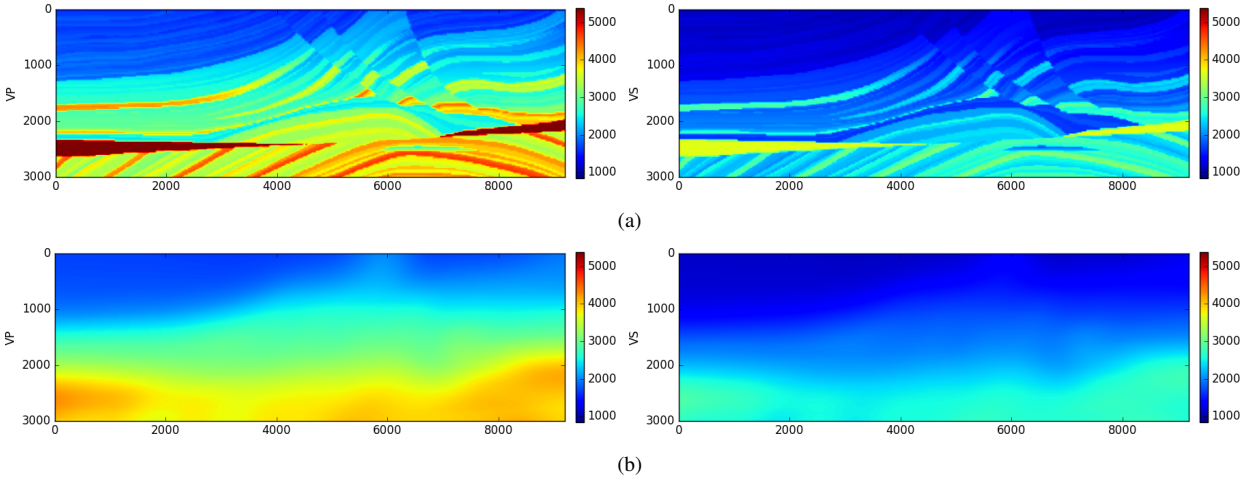


Figure 1. The (a) true and (b) initial elastic Marmousi models used in elastic FWI.

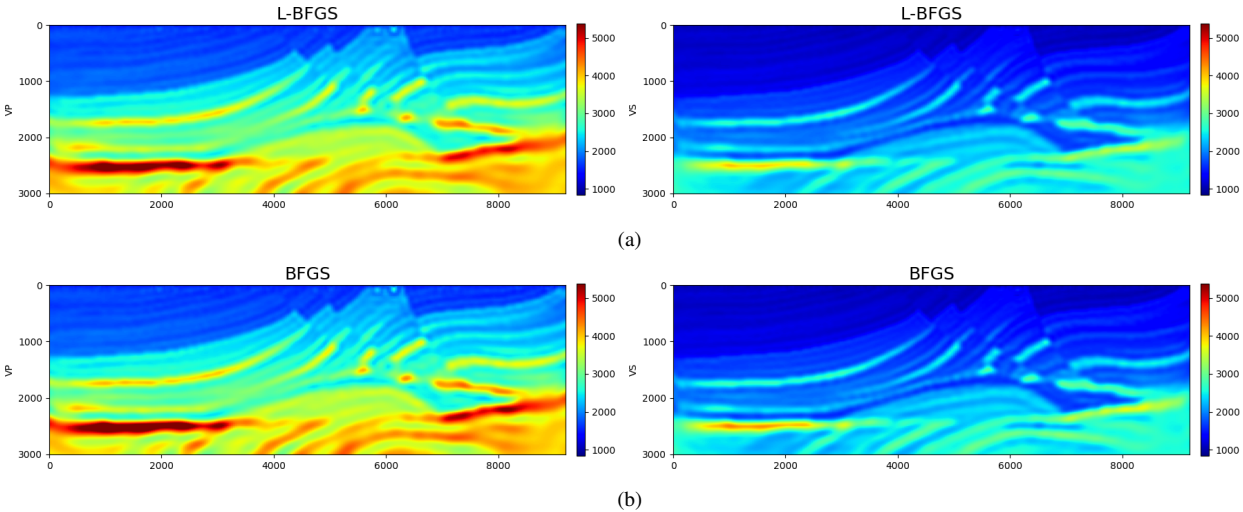


Figure 2. Inverted models from elastic FWIs using (a) L-BFGS and (b) BFGS after 82 and 65 iterations. L-BFGS runs with 5 memories; BFGS runs in the L-BFGS flow but with all the memories. The results look similar even with different iterations.

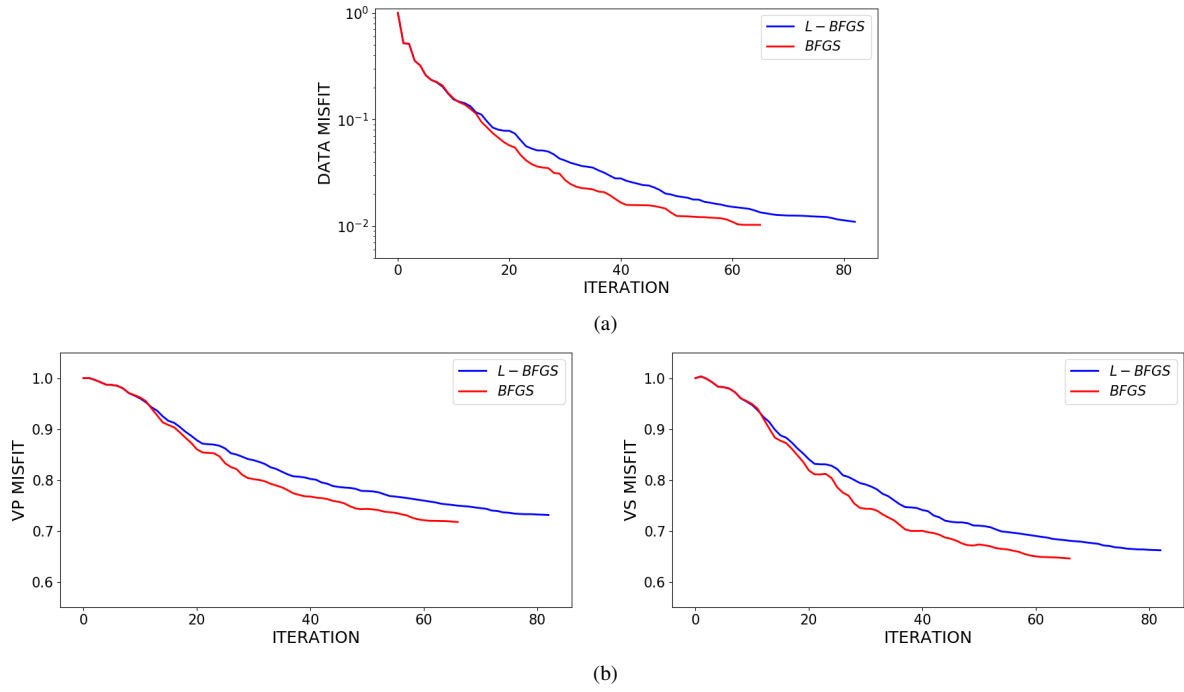


Figure 3. Convergence rates of L-BFGS- and BFGS-based elastic FWIs. Plotted are (a) data-misfit and (b) model-misfit comparisons.

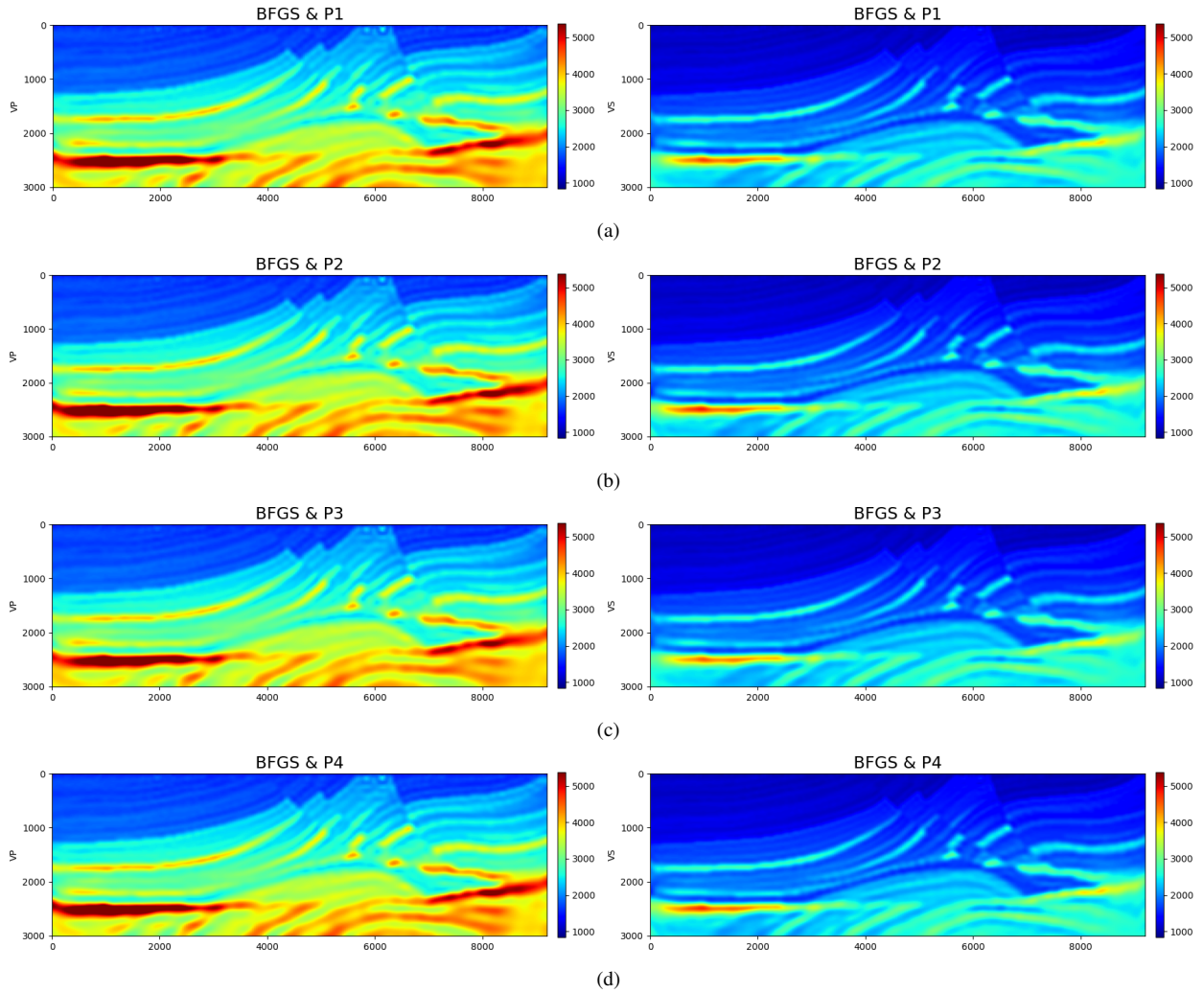


Figure 4. From top to bottom: inverted results of BFGS-based FWIs with four different preconditioners after 59, 48, 46, 79 iterations. Among them, (d) is closest to the true model (left panel: V_P , right panel: V_S velocities).

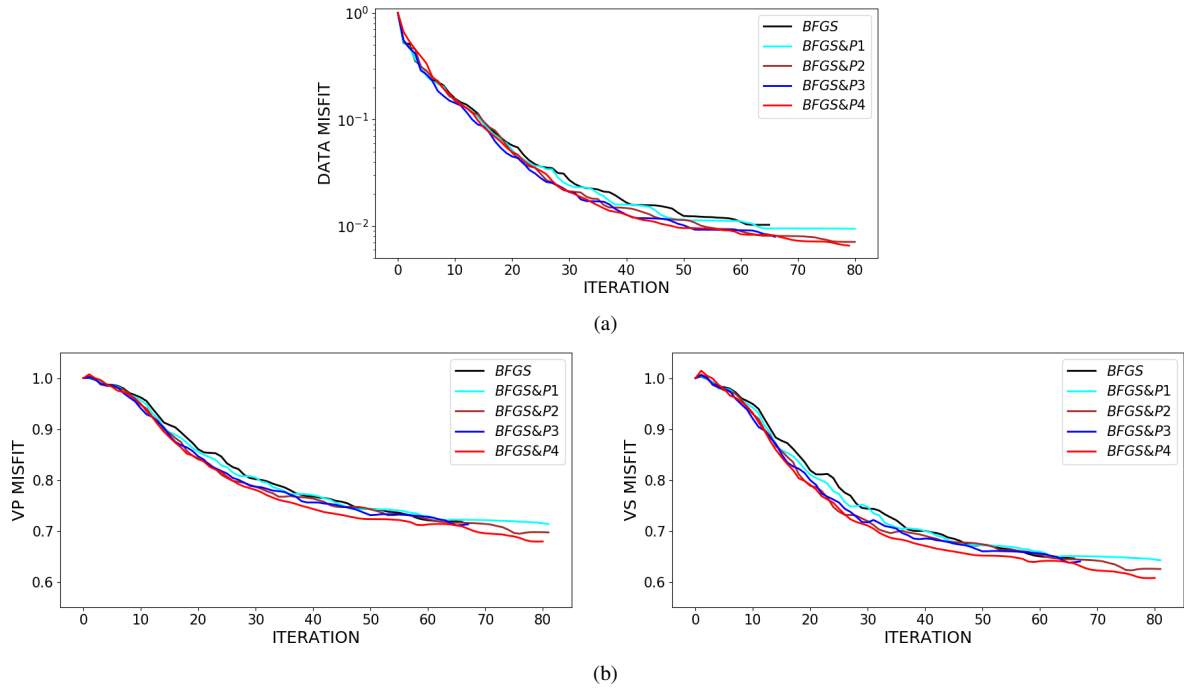


Figure 5. Convergence rate comparisons of preconditioned BFGS-based FWIs, with the pure BFGS-based in black for reference. Plotted in (a) and (b) are data-misfit and model-misfit convergence curves, respectively.

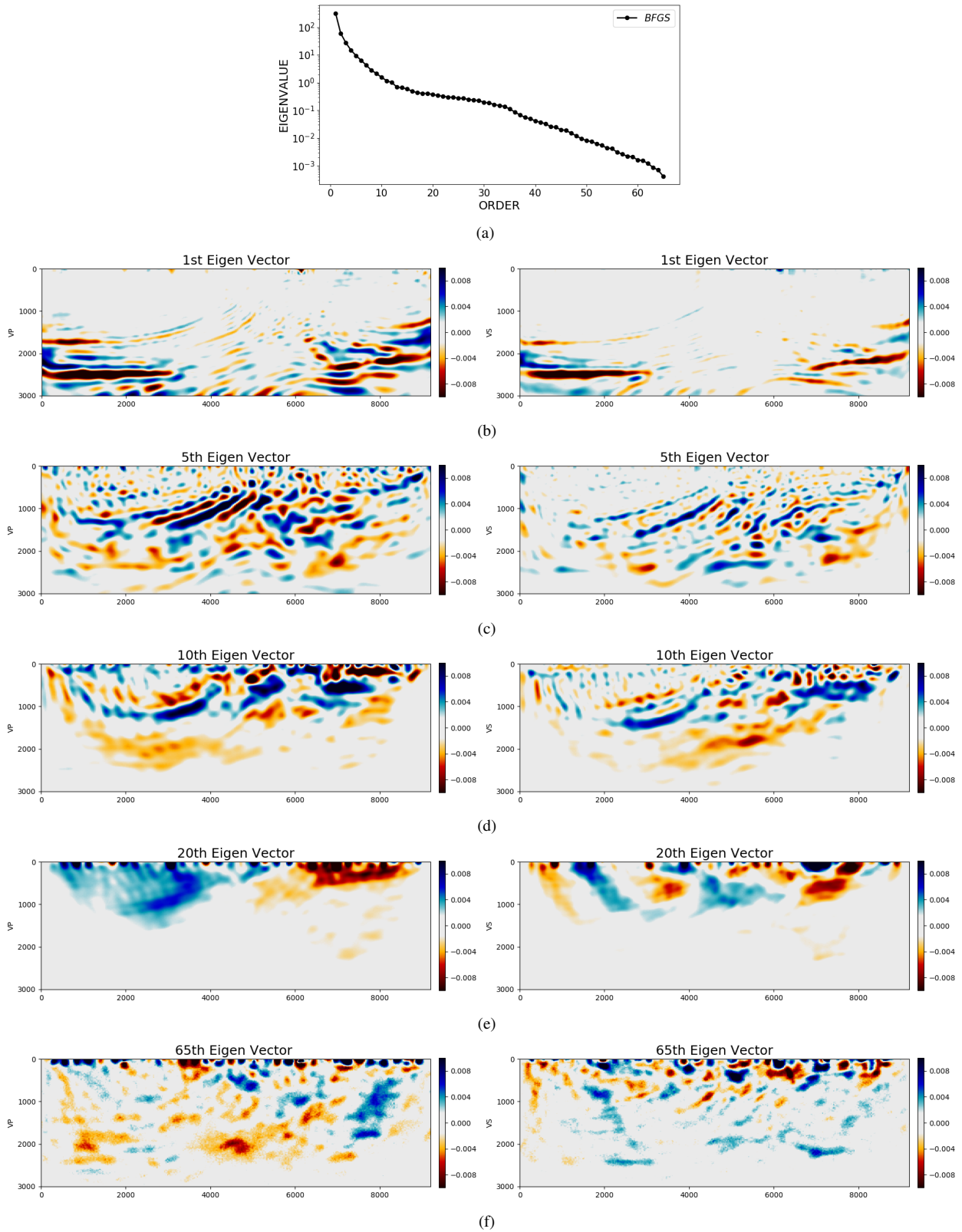


Figure 6. Eigendecomposition of the inverse Hessian from the BFGS-based elastic FWI using randomized SVD. Plotted in (a) is the eigenvalues in logarithmic scale. Plotted in the rest are the 1st, 5th, 10th, 20th, and the final eigenvectors (left panel: V_P , right panel: V_S velocities), respectively.

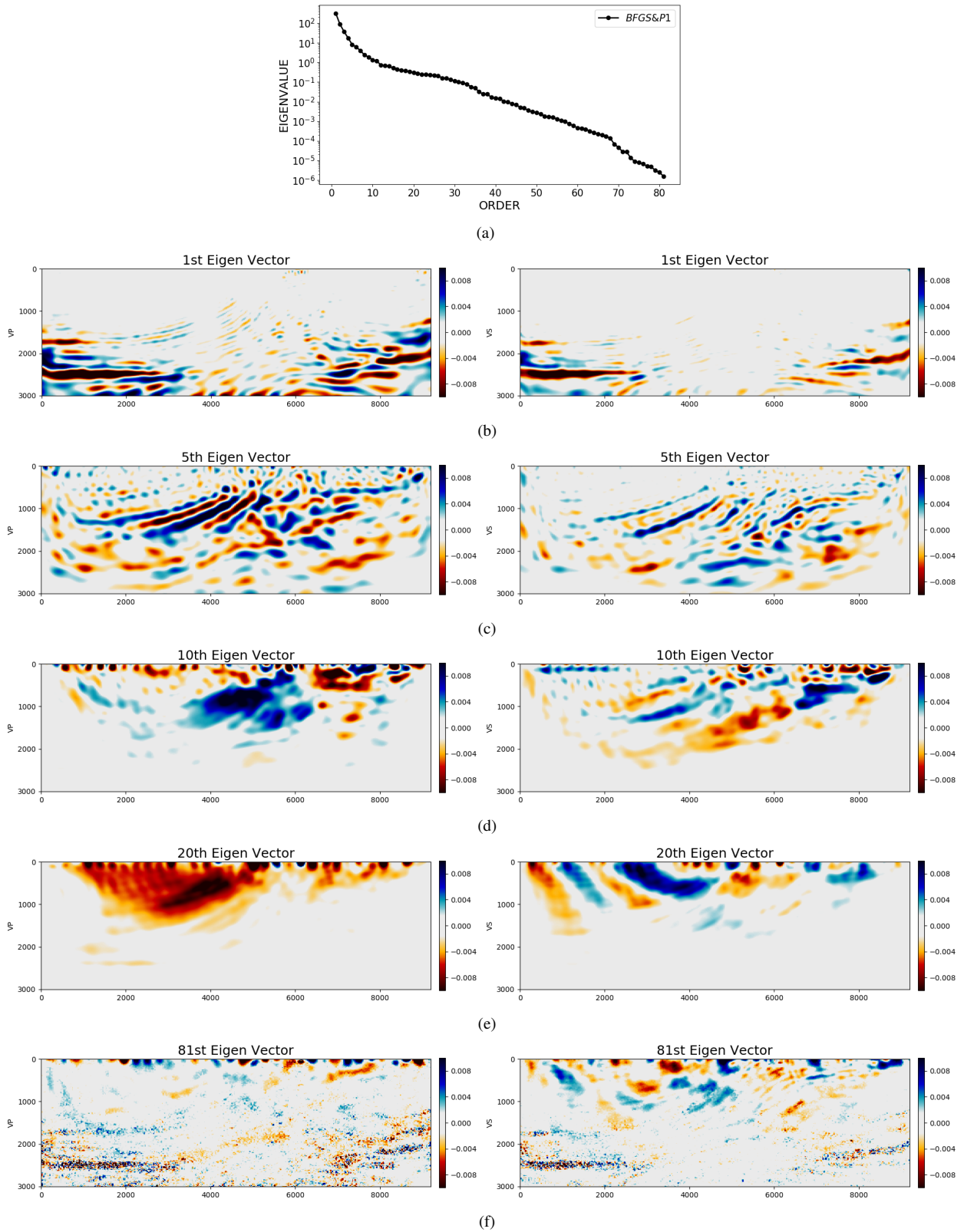


Figure 7. Eigendecomposition of the inverse Hessian from the BFGS & P1 elastic FWI using randomized SVD. Plotted in (a) is the eigenvalues in logarithmic scale. Plotted in the rest are the 1st, 5th, 10th, 20th, and the final eigenvectors (left panel: V_P , right panel: V_S velocities), respectively.

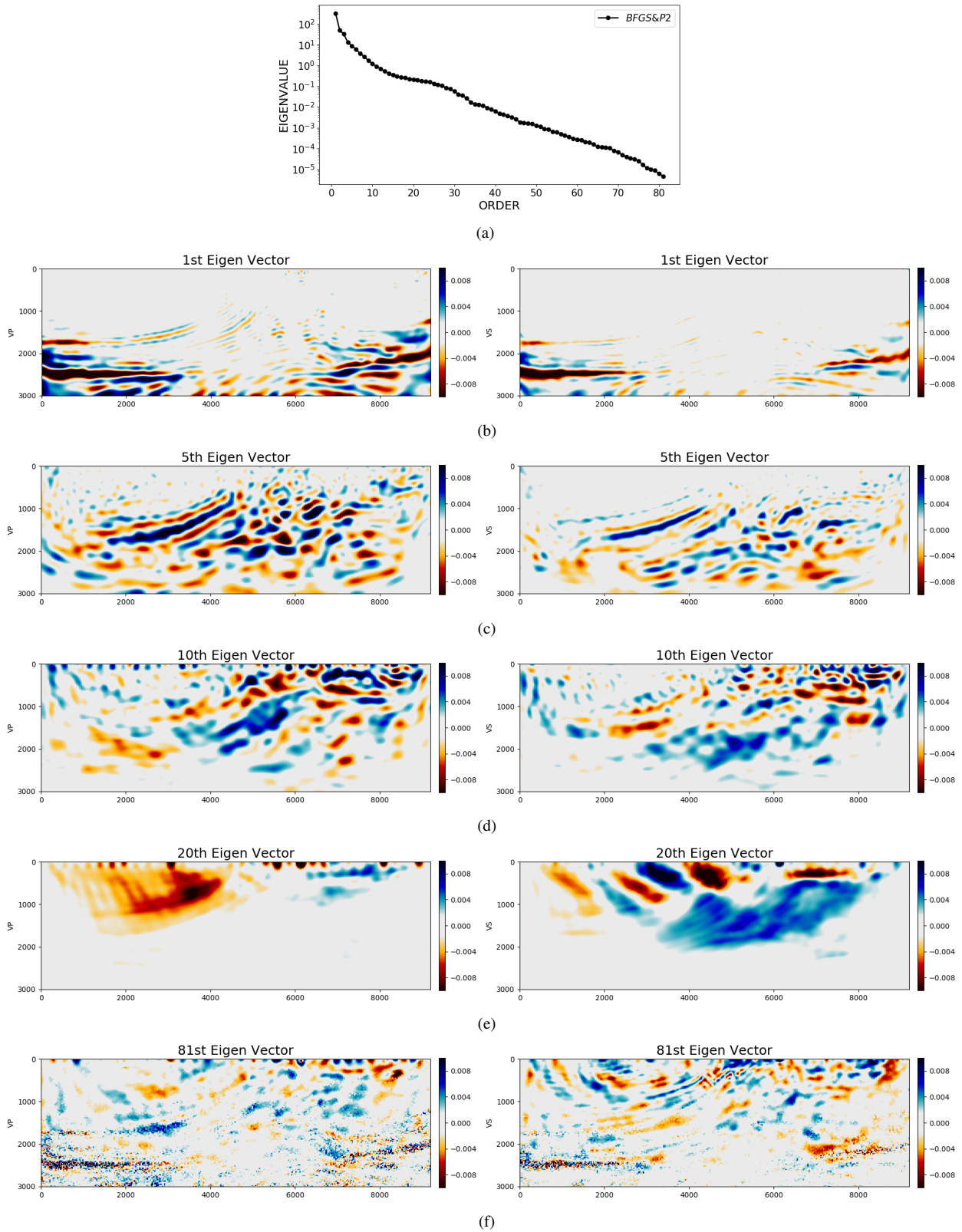


Figure 8. Eigendecomposition of the inverse Hessian from the BFGS & P2 elastic FWI using randomized SVD. Plotted in (a) is the eigenvalues in logarithmic scale. Plotted in the rest are the 1st, 5th, 10th, 20th, and the final eigenvectors (left panel: V_P , right panel: V_S velocities), respectively.

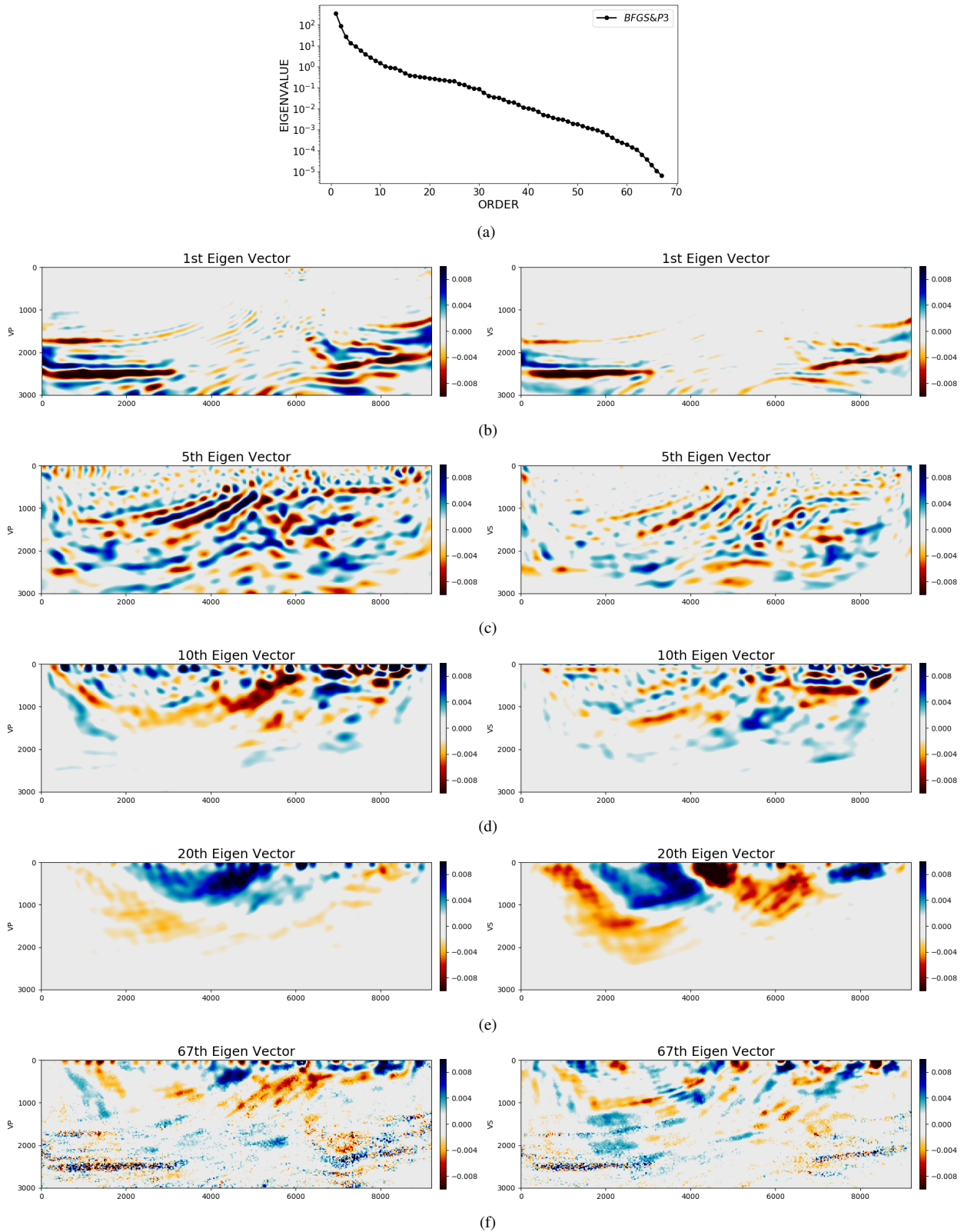


Figure 9. Eigendecomposition of the inverse Hessian from the BFGS & P3 elastic FWI using randomized SVD. Plotted in (a) is the eigenvalues in logarithmic scale. Plotted in the rest are the 1st, 5th, 10th, 20th, and the final eigenvectors (left panel: V_P , right panel: V_S velocities), respectively.

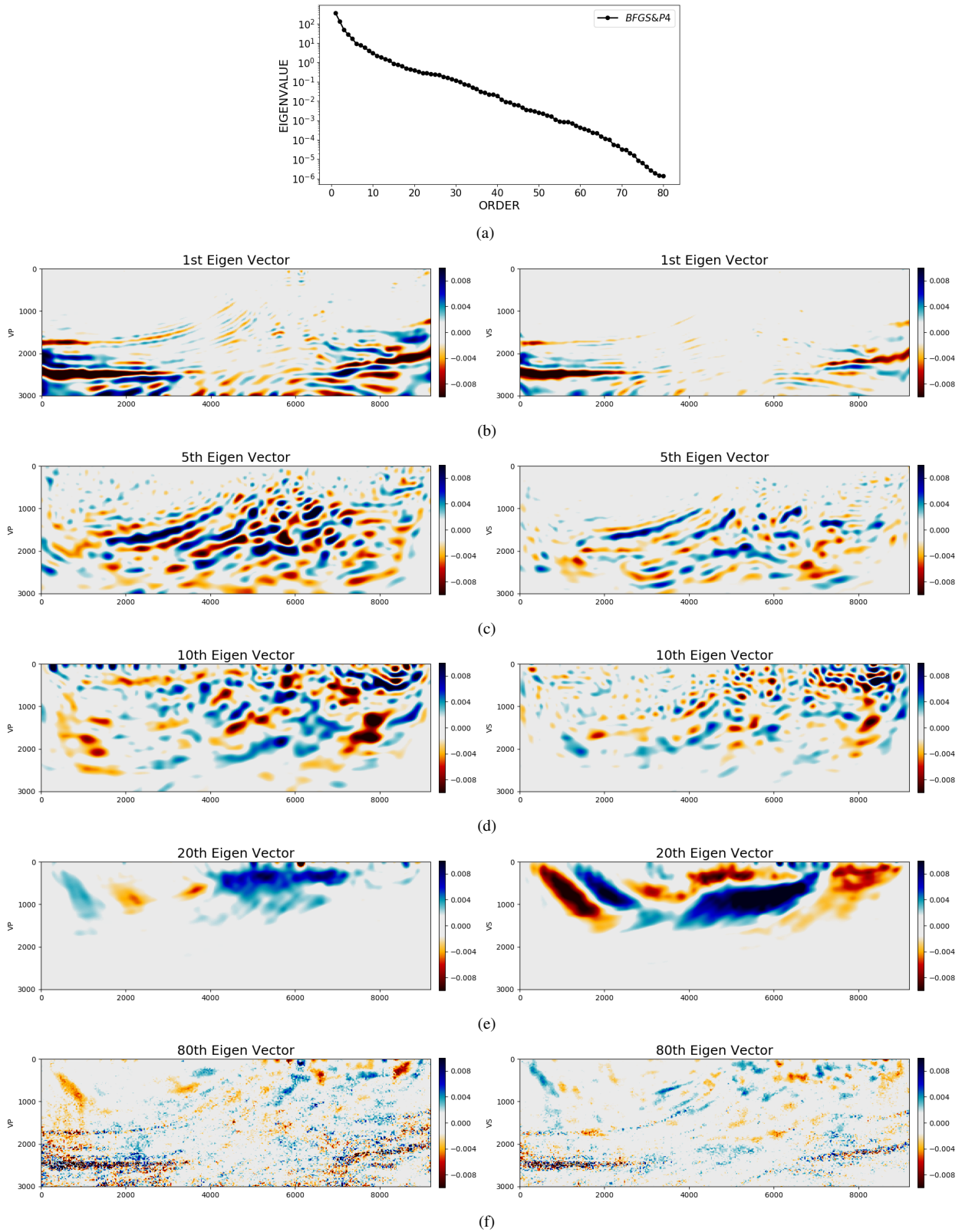


Figure 10. Eigendecomposition of the inverse Hessian from the BFGS & P4 elastic FWI using randomized SVD. Plotted in (a) is the eigenvalues in logarithmic scale. Plotted in the rest are the 1st, 5th, 10th, 20th, and the final eigenvectors (left panel: V_P , right panel: V_S velocities), respectively.

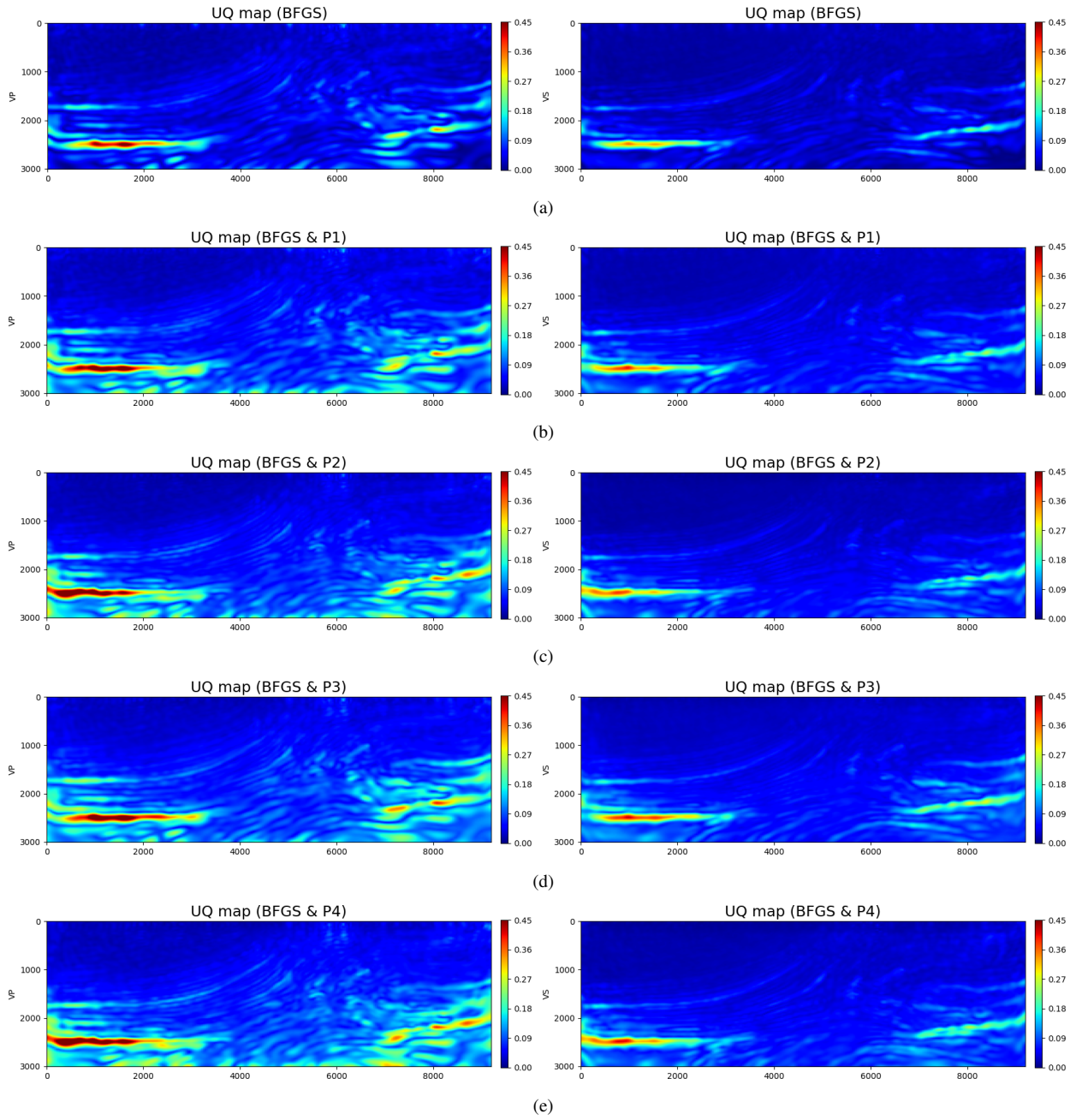


Figure 11. Uncertainty Quantification maps for elastic FWIs using BFGS, and preconditioned BFGSs, as shown from top to bottom (left panel: V_P , right panel: V_S velocities).

APPENDIX A: DERIVATION OF THE DIAGONAL HESSIANS WITH THE ADJOINT METHOD

FWI aims to minimize the following misfit function

$$f(\mathbf{m}) = \frac{1}{2} \|\mathbf{d}(\mathbf{m}) - \mathbf{d}_0\|_2^2, \quad (\text{A1})$$

in which \mathbf{d}_0 is the observed data, and $\mathbf{d}(\mathbf{m}) = \mathbf{R}\mathbf{u}(\mathbf{m})$ the simulated data, with $\mathbf{u}(\mathbf{m})$ the simulated data from model \mathbf{m} and \mathbf{R} the acquisition sampling operator. Under the Born approximation $\mathbf{m} = \mathbf{m}_0 + \delta\mathbf{m}$, we have

$$\mathbf{d}(\mathbf{m}_0 + \delta\mathbf{m}) = \mathbf{d}(\mathbf{m}_0) + \mathbf{J}\delta\mathbf{m} + O(\delta\mathbf{m}^2), \quad (\text{A2})$$

with Jacobian matrix $\mathbf{J} = \delta\mathbf{d}/\delta\mathbf{m}$. Taking the first-order derivative of eq. (A1) yields

$$\frac{\partial f}{\partial \mathbf{m}} = \mathbf{J}^\dagger [\mathbf{J}(\mathbf{m}_0 + \delta\mathbf{m}) - \mathbf{d}_0] = \mathbf{J}^\dagger (\mathbf{J}\delta\mathbf{m} - \delta\mathbf{d}), \quad (\text{A3})$$

with $\delta\mathbf{d} = \mathbf{d}_0 - \mathbf{J}\mathbf{m}_0$ and \dagger the adjoint of an operator. When $\partial f/\partial \mathbf{m} = 0$, we have a direct solution to model perturbation $\delta\mathbf{m}$ as

$$\delta\mathbf{m} = (\mathbf{J}^\dagger \mathbf{J})^{-1} \mathbf{J}^\dagger \delta\mathbf{d}, \quad (\text{A4})$$

in which, however, the Hessian $\mathbf{H} = \mathbf{J}^\dagger \mathbf{J}$ is prohibitive to calculate, store, and invert. Hence, in practical applications, we simply calculate the gradient as

$$\delta\mathbf{m}^* = \mathbf{J}^\dagger \delta\mathbf{d}, \quad (\text{A5})$$

For convenience everything is written in a velocity-stress formulation even though we're using SPECFEM which is not solving this specific system. The 2D velocity-stress isotropic elastic wave equation reads (Vigh et al. 2014; Chen & Sacchi 2017)

$$\begin{pmatrix} \rho \mathbf{I} & \mathbf{0} \\ \mathbf{0} & \mathbf{I} \end{pmatrix} \frac{\partial \mathbf{u}}{\partial t} - \begin{pmatrix} \mathbf{0} & \mathbf{D}^T \\ \mathbf{CD} & \mathbf{0} \end{pmatrix} \mathbf{u} = \mathbf{s}, \quad (\text{A6})$$

where \mathbf{s} is the source term, \mathbf{I} the identity matrix, and

$$\mathbf{u} = (\mathbf{v}, \sigma), \mathbf{v} = (v_x, v_z)^T, \sigma = (\sigma_{xx}, \sigma_{xz}, \sigma_{zz})^T, \quad (\text{A7})$$

$$\mathbf{C} = \begin{pmatrix} \lambda + 2\mu & \lambda & 0 \\ \lambda & \lambda + 2\mu & 0 \\ 0 & 0 & \mu \end{pmatrix}, \mathbf{D} = \begin{pmatrix} \partial/\partial x & 0 \\ 0 & \partial/\partial z \\ \partial/\partial z & \partial/\partial x \end{pmatrix}$$

with \mathbf{v} the particle velocities, σ the stress tensors, \mathbf{C} the isotropic elastic tensor with λ and μ being the Lamé parameters, \mathbf{D} the operator of spatial derivatives, and the initial condition of $\mathbf{u}(\mathbf{x}, t | t < 0) = \mathbf{0}$. To avoid notation clustering, we drop out the spatial and temporal dependence (\mathbf{x}, t) of \mathbf{u} and the spatial dependence (\mathbf{x}) of \mathbf{C} . Eq. (A7) is the state equation when FWI runs as an optimal control problem (Tromp et al. 2005; Plessix 2006). For simplification, the abstract form of eq. (A7) reads

$$\mathbf{A}\mathbf{u} = \mathbf{s}, \quad (\text{A8})$$

and its first-order derivative over \mathbf{m} reads

$$\mathbf{A} \frac{\partial \mathbf{u}}{\partial \mathbf{m}} = -\frac{\partial \mathbf{A}}{\partial \mathbf{m}} \mathbf{u}. \quad (\text{A9})$$

Then, the \mathbf{J} in eq. (A2) can be recast as

$$\mathbf{J} = \frac{\partial \mathbf{d}}{\partial \mathbf{m}} = \mathbf{R} \frac{\partial \mathbf{u}}{\partial \mathbf{m}} = -\mathbf{R}\mathbf{A}^{-1} \frac{\partial \mathbf{A}}{\partial \mathbf{m}} \mathbf{u}, \quad (\text{A10})$$

in which \mathbf{A}^{-1} is the Green's operator given that $\mathbf{u} = \mathbf{A}^{-1}\mathbf{s}$. Then, the gradient from the data residual can be rewritten in details (Tarantola 1988) as

$$\delta \mathbf{m}^* = \mathbf{J}^\dagger \delta \mathbf{d} = \left(-\mathbf{R}\mathbf{A}^{-1} \frac{\partial \mathbf{A}}{\partial \mathbf{m}} \mathbf{u} \right)^\dagger \delta \mathbf{d} = -\left(\frac{\partial \mathbf{A}}{\partial \mathbf{m}} \mathbf{u} \right)^\dagger (\mathbf{A}^\dagger)^{-1} \mathbf{R}^\dagger \delta \mathbf{d}, \quad (\text{A11})$$

which represents the mapping from data residual $\delta \mathbf{d}$ to the gradient \mathbf{J} via the adjoint operator \mathbf{J}^\dagger . By introducing the adjoint-state variable $\tilde{\mathbf{u}}$ from the following equation

$$\mathbf{A}^\dagger \tilde{\mathbf{u}} = \mathbf{R}^\dagger \delta \mathbf{d}, \quad (\text{A12})$$

and its corresponding elastic wave equation can be expressed as

$$\begin{pmatrix} \rho \mathbf{I} & \mathbf{0} \\ \mathbf{0} & \mathbf{I} \end{pmatrix} \left(\frac{\partial}{\partial t} \right)^\dagger \tilde{\mathbf{u}} - \begin{pmatrix} \mathbf{0} & \mathbf{D}^T \\ \mathbf{C}\mathbf{D} & \mathbf{0} \end{pmatrix}^\dagger \tilde{\mathbf{u}} = \mathbf{R}^\dagger \delta \mathbf{d}, \quad (\text{A13})$$

where $\mathbf{R}^\dagger \delta \mathbf{d}$ acts as the adjoint sources. After the operators of the adjoint \dagger are applied, Eq. (A13) can be recast as

$$\begin{pmatrix} \rho \mathbf{I} & \mathbf{0} \\ \mathbf{0} & \mathbf{I} \end{pmatrix} \left(-\frac{\partial}{\partial t} \right) \tilde{\mathbf{u}} + \begin{pmatrix} \mathbf{0} & \mathbf{D}^T \mathbf{C} \\ \mathbf{D} & \mathbf{0} \end{pmatrix} \tilde{\mathbf{u}} = \mathbf{R}^\dagger \delta \mathbf{d}, \quad (\text{A14})$$

The term $\delta\sigma$ in $\delta\mathbf{d} = (\delta\mathbf{v}, \delta\sigma)$ stays as zero because we only observe $\delta\mathbf{v}$ in practice. The final form of the adjoint-state equation (Vigh et al. 2014) is recast as

$$\begin{pmatrix} \rho\mathbf{I} & \mathbf{0} \\ \mathbf{0} & \mathbf{I} \end{pmatrix} \left(-\frac{\partial}{\partial t}\right) \tilde{\mathbf{u}} + \begin{pmatrix} \mathbf{0} & \mathbf{D}^T \\ \mathbf{C}\mathbf{D} & \mathbf{0} \end{pmatrix} \tilde{\mathbf{u}} = \mathbf{R}^\dagger \begin{pmatrix} \delta\mathbf{v} \\ \mathbf{0} \end{pmatrix}, \quad (\text{A15})$$

Let us look back to the gradient in eq. (A5), which can be further expressed as

$$\delta\mathbf{m}^* = -\left(\frac{\partial\mathbf{A}}{\partial\mathbf{m}}\mathbf{u}\right)^\dagger \tilde{\mathbf{u}}, \quad (\text{A16})$$

or in an explicit form as

$$\delta\mathbf{m}(\mathbf{x})^* = -\int \left(\frac{\partial\mathbf{A}}{\partial\mathbf{m}}\mathbf{u}\right)^\dagger \tilde{\mathbf{u}} dt = -\int \left(\frac{\partial\mathbf{A}}{\partial\mathbf{m}}\mathbf{u}\right) \tilde{\mathbf{u}}^T dt, \quad (\text{A17})$$

with $\tilde{\mathbf{u}}(\mathbf{x}, t)^T = \tilde{\mathbf{u}}(\mathbf{x}, t)^\dagger$ applied. Eq. (A17) is also well known in the sense of reverse-time migration (Baysal et al. 1983) with the adjoint method.

When computing the gradients, we may have different parametrizations, such as (α, β, ρ) or (λ, μ, ρ) , with α, β, ρ being the P- and S-wave velocities, and densities, λ, μ being Lamé parameters, respectively. We exemplify the gradients with respect to (α, β, ρ) as following

$$\begin{aligned} \delta\alpha^* &= \int \left(\frac{\partial\mathbf{C}}{\partial\alpha}\mathbf{D}\mathbf{v}\right) \cdot \tilde{\sigma} dt, \\ \delta\beta^* &= \int \left(\frac{\partial\mathbf{C}}{\partial\beta}\mathbf{D}\mathbf{v}\right) \cdot \tilde{\sigma} dt, \\ \delta\rho^* &= -\int \frac{\partial\mathbf{v}}{\partial t} \cdot \tilde{\mathbf{v}} dt. \end{aligned} \quad (\text{A18})$$

When looking back to eq. (A4). we see the hope of accelerating FWI with the Hessian in Gauss-Newton approximation, which has the form of

$$\mathbf{H} = \mathbf{J}^\dagger \mathbf{J} = \left(\mathbf{R}\mathbf{A}^{-1}\frac{\partial\mathbf{A}}{\partial\mathbf{m}}\mathbf{u}\right)^\dagger \left(\mathbf{R}\mathbf{A}^{-1}\frac{\partial\mathbf{A}}{\partial\mathbf{m}}\mathbf{u}\right), \quad (\text{A19})$$

in which \mathbf{A}^{-1} resembles the Green's operator and \mathbf{u} the source wavefield. Regardless of the band-limited source wavelet, \mathbf{u} resembles the source-side Green's functions \mathbf{G}_S , and at the same time, $\mathbf{R}\mathbf{A}^{-1}$ the receiver-side Green's functions \mathbf{G}_R .

The full computation and storage of \mathbf{H} are also prohibitive. Therefore, Shin et al. (2008) propose to forget \mathbf{G}_R to save the computational cost, and only compute the Hessian diagonals via zero-lag cross-correlation of the source wavefields as follows

$$\mathbf{H}(\mathbf{x}, \mathbf{x}) = \int \left(\frac{\partial\mathbf{C}}{\partial m_i}\mathbf{D}\mathbf{v}(\mathbf{x})\right) \cdot \left(\frac{\partial\mathbf{C}}{\partial m_i}\mathbf{D}\mathbf{v}(\mathbf{x})\right) dt. \quad (\text{A20})$$

When it comes to parametrization (α, β, ρ) , we have

$$\begin{aligned}
H_{\alpha\alpha} &= \int \left(\frac{\partial \mathbf{C}}{\partial \alpha} \mathbf{D}\mathbf{v} \right) \cdot \left(\frac{\partial \mathbf{C}}{\partial \alpha} \mathbf{D}\mathbf{v} \right) dt = 8\rho^2 \alpha^2 \int \left(\frac{\partial v_x}{\partial x} + \frac{\partial v_z}{\partial z} \right)^2 dt, \\
H_{\beta\beta} &= \int \left(\frac{\partial \mathbf{C}}{\partial \beta} \mathbf{D}\mathbf{v} \right) \cdot \left(\frac{\partial \mathbf{C}}{\partial \beta} \mathbf{D}\mathbf{v} \right) dt = 16\rho^2 \alpha^2 \int \left[\left(\frac{\partial v_x}{\partial x} \right)^2 + \left(\frac{\partial v_z}{\partial z} \right)^2 \right] dt + 4\rho^2 \beta^2 \int \left(\frac{\partial v_z}{\partial x} + \frac{\partial v_x}{\partial z} \right)^2 dt, \\
H_{\rho\rho} &= \int \left(\frac{\partial \mathbf{v}}{\partial t} \right) \cdot \left(\frac{\partial \mathbf{v}}{\partial t} \right) dt = \int \left[\left(\frac{\partial v_x}{\partial t} \right)^2 + \left(\frac{\partial v_z}{\partial t} \right)^2 \right] dt,
\end{aligned} \tag{A21}$$

with \mathbf{v} being the source wavefield in particle velocities. Eq. (A21), however, does not involve the receiver-side Green's functions. Following Luo (2012), we modify eq. (A21) to include \mathbf{G}_R as

$$\begin{aligned}
\tilde{H}_{\alpha\alpha} &= \left| \int \left(\frac{\partial \mathbf{C}}{\partial \alpha} \mathbf{D}\mathbf{v} \right) \cdot \left(\frac{\partial \mathbf{C}}{\partial \alpha} \mathbf{D}\tilde{\mathbf{v}} \right) dt \right| = 8\rho^2 \alpha^2 \left| \int \left(\frac{\partial v_x}{\partial x} + \frac{\partial v_z}{\partial z} \right) \left(\frac{\partial \tilde{v}_x}{\partial x} + \frac{\partial \tilde{v}_z}{\partial z} \right) dt \right|, \\
\tilde{H}_{\beta\beta} &= \left| \int \left(\frac{\partial \mathbf{C}}{\partial \beta} \mathbf{D}\mathbf{v} \right) \cdot \left(\frac{\partial \mathbf{C}}{\partial \beta} \mathbf{D}\tilde{\mathbf{v}} \right) dt \right| \\
&= 16\rho^2 \alpha^2 \left| \int \left(\frac{\partial v_x}{\partial x} \frac{\partial \tilde{v}_x}{\partial x} + \frac{\partial v_z}{\partial z} \frac{\partial \tilde{v}_z}{\partial z} \right) dt \right| + 4\rho^2 \beta^2 \left| \int \left(\frac{\partial v_z}{\partial x} + \frac{\partial v_x}{\partial z} \right) \left(\frac{\partial \tilde{v}_z}{\partial x} + \frac{\partial \tilde{v}_x}{\partial z} \right) dt \right|, \\
\tilde{H}_{\rho\rho} &= \left| \int \left(\frac{\partial \mathbf{v}}{\partial t} \right) \cdot \left(\frac{\partial \tilde{\mathbf{v}}}{\partial t} \right) dt \right|,
\end{aligned} \tag{A22}$$

with the new $\tilde{\mathbf{v}}$ being the adjoint wavefield in particle velocities. We take their absolute values to ensure the positive definiteness of the Hessian initial.